Eindhoven University of Technology

MASTER

Experimental and Numerical Approach to Blast Furnace Hearth Dynamics
Fluid flow with Heat and Mass Transport

Manjunath, V.

Award date:
2020

[Link to publication](#)

Disclaimer
This document contains a student thesis (bachelor's or master's), as authored by a student at Eindhoven University of Technology. Student theses are made available in the TU/e repository upon obtaining the required degree. The grade received is not published on the document as presented in the repository. The required complexity or quality of research of student theses may vary by program, and the required minimum study period may vary in duration.

General rights
Copyright and moral rights for the publications made accessible in the public portal are retained by the authors and/or other copyright owners and it is a condition of accessing publications that users recognise and abide by the legal requirements associated with these rights.

- Users may download and print one copy of any publication from the public portal for the purpose of private study or research.
- You may not further distribute the material or use it for any profit-making activity or commercial gain

Department of Chemical Engineering and Chemistry
Multiphase Reactors Group - Multi-Scale Modelling of Multiphase Flows

Experimental and Numerical Approach to Blast Furnace Hearth Dynamics

Fluid flow with Heat and Mass Transport

Master Thesis
V. Manjunath, *B.Eng*

Graduation Committee:
Prof.dr.ir. Hans A.M. Kuipers
Dr.ir. Kay A. Buist
Dr. Giulia Finotello
Ir. Tim M.J. Nijssen

Eindhoven, May 2020

Abstract

The blast furnace is a complex counter current reactor which stands at the heart of one of biggest industrial processes of our modern society, steelmaking. The campaign life time of a blast furnace is highly influenced by its hearth. In order to understand the dynamics of the blast furnace hearth, this work focuses on the fluid flow, heat and mass transfer in the hearth. A CFD-DEM model was adopted where the particles are modelled by Discrete Element Method (DEM) while the fluid phase was modelled by Volume of Fluid method (VOF). A four way coupling was implemented through CFDEMCoupling. Apart from the model, experiments were conducted to evaluate the fluid flow and bed dynamics in a cold hearth system.

The experiments focused on the the influence of inflow rates on the bed dynamics. The experimental data was used to validate a flow model and further analysis was done to obtain the fluid flow profiles in the system. The fluid profiles were utilized to roughly estimate the common wear found in the hearth walls. During experiments, it was observed that the particles in the bed migrated over time. Further these migrations increased with the rate of the fluid inflow.

Heat transfer between the particles and fluid is analysed along with granular heat conduction in solids. The model provides good results for the heat transfer in an adiabatic packed bed.An analysis of heat transfer through the walls was also performed. However, results are not yet in correspondence with literature data.

Analogous to the heat transfer model, mass transfer models are developed. The model also predicts the change in particle size as it dissolves in the fluid. The model's predictions of particle to fluid mass transfer is closely comparable to the analytical solution. Further, the VOF models are corrected to account for the diffusion at the interface by the thermodynamic equilibrium of chemical species at the interface.

Contents

Contents v

List of Figures vii

List of Tables ix

1 Introduction 1
- 1.1 Iron and Steel Industry 1
- 1.2 Blast Furnace 2
  - 1.2.1 Hearth and Deadman 3
- 1.3 Subject of Research 4

2 Literature Survey 5
- 2.1 Early attempts at understanding Dynamics of Blast Furnace 5
- 2.2 Mathematical model of Iron making process 6
  - 2.2.1 Four-Fluid Model of Blast Furnace 6
  - 2.2.2 CFD-DEM model of Blast Furnace 6
- 2.3 Heat transfer 7
- 2.4 Mass Transfer 9

3 Methodology - Experimental 11
- 3.1 Material Properties 11
- 3.2 Experimental Setup 12
  - 3.2.1 Hearth 12
  - 3.2.2 Deadman 12
  - 3.2.3 Fluid flow 13
  - 3.2.4 Burden Force 13
  - 3.2.5 Raceway and Particle Recycle 14
- 3.3 Particle Dynamics 14
  - 3.3.1 Bed movement 14
  - 3.3.2 Magnetic Particle Tracking 14
- 3.4 Flow Experiments 16

4 Methodology - Modelling 17
- 4.1 Computational Fluid Dynamics 17
- 4.2 Volume of Fluid (VOF) 18
- 4.3 Discrete Element Method 18
- 4.4 CFD - DEM Coupling 19
- 4.5 Heat transfer in Blast furnace hearth 22
  - 4.5.1 Heat transfer between the particles 22
  - 4.5.2 Particle - Fluid Heat transfer 23
  - 4.5.3 Heat transfer through conduction 23
  - 4.5.4 Wall heat transfer 23

4.6 Mass transfer in Blast Furnace Hearth . . . 25
  4.6.1 Diffusion and Correction for diffusion . . . 25
  4.6.2 Mass Transfer between Solid and Fluid phases . . . 25
  4.6.3 Shrinking of Particles . . . 26

5 Experimental Results and Discussions **27**
5.1 Fluid flow . . . 27
5.2 Force controller calibration . . . 27
5.3 Moving bed and Particle position . . . 28
5.4 Fluid flow and particle migration . . . 29

6 Numerical Results and Discussions **33**
6.1 Blast furnace hearth simulations . . . 33
  6.1.1 Model validation . . . 35
  6.1.2 Flow profiles and Circumferential flow . . . 36
  6.1.3 Floating bed and fluid flow . . . 37
  6.1.4 Influence of inlet flow rates . . . 38
6.2 Heat Transfer . . . 41
  6.2.1 Adiabatic heat transfer model . . . 41
  6.2.2 Non adiabatic - Heat transfer through walls . . . 43
6.3 Mass transfer . . . 47
  6.3.1 Single fluid mass transfer model . . . 47
  6.3.2 Mass transfer at fluid interface . . . 49

7 Conclusions **51**

8 Future perspective **53**

Bibliography **57**

List of Figures

1.1 Global crude steel production over the years [1] 1
1.2 Blast furnace Cross section with zones and temperatures 2
1.3 (a) Hearth section of the blast furnace; (b) "Elephant foot" corrosion profile for a carbon based crucible [2] 3

2.1 Dig-out of the Kokura 2 Blast Furnace [3] 5
2.2 (a) Representation of the four fluids in the packed bed; (b) Phase fractions in the bed with G - Gas, S - Solid, F - Fine powder, L - Liquid; (c) Interactions between the phases of the model [4]. 6
2.3 Snapshots of the blast furnace hearth at three different times. The columns represent from left to right t = 0 s , t = 5 s and t = 20 s . The first row shows the deadman and the force walls, the second and the third row depicts the velocity field at Plane y and Plane z respectively. The white lines visualize the air-slag (upper) and iron-slag (lower) interfaces. [5] 7
2.4 Calculated predictions of temperature profiles in the BF hearth walls. [6] 8

3.1 (a)Experimental setup of the hearth with MPT system and different components. . 11
3.2 Particle size distribution 12
3.3 Vessel representing the hearth 12
3.4 (a) Cylindrical vessel representing the hearth and tapholes (b) Inlet route for the water (c) Burden plate that applies force on the bed. 13
3.5 Magnetic Particle Tracking system with a total of 72 sensors split over 4 discs. . . 15

4.1 Simple spring dashpot model 18
4.2 left:flow around the particle is resolved; right:unresolved CFD where flow around the particles is modelled. 20

5.1 Analysing the inflow and outflow rates of the experimental runs; (a) Inflow rate = 0.75 L·min^{-1}; (b) Inflow rate = 1.00 L·min^{-1}; (c) Inflow rate = 1.25 L·min^{-1}; . . 27
5.2 Optimisation of PID control for burden plate movement with different values for the parameters of equation 5.1; The results of selected parameters are shown on the right. 28
5.3 (a) Comparing the level of water in system to the axial position of particle and burden plate with time to analyse the movement of bed and the plate. 29
5.4 Comparing axial particle positions with different inflow rates of water; (a) Inflow rate = 0.75 L·min^{-1}; (b) Inflow rate = 1.00 L·min^{-1}; (c) Inflow rate = 1.25 L·min^{-1}; 31
5.5 Comparing radial particle positions with different inflow rates of water; (a) Inflow rate = 0.75 L·min^{-1}; (b) Inflow rate = 1.00 L·min^{-1}; (c) Inflow rate = 1.25 L·min^{-1}; 31

6.1 Mesh and geometry of the hearth used for the simulations with the geometry similar to the experimental setup with inlets and tapholes. 33

6.2 (a) Comparing the results of the simulation with the level of water present in the system during experiments; (b) Comparing the axial particle position as recorded by MPT and the results of the simulation. 35
6.3 Comparing the influence of inflow rate on particle migration inside the bed; (Left) Axial migration of the particle in the bed; (Right) Radial migration of the particle in the bed. 36
6.4 (a) Velocity profile of water in a horizontal plane at the height of the taphole. (b) Velocity profile of water in a xz plane when the water level is at 6cm height from the bottom. 37
6.5 (a) Void fraction in the system to illustrate the particle free space at the bottom (b) Velocity profile of water in a xz plane where the velocity of water is maximum in the particle free space. 38
6.6 (a) Velocity profile of fluid during tapping with the coke particles providing resistance to the flow (b) Velocity profile of water in a xz plane where the velocity of water is unrestricted by the bed of particles. 38
6.7 Comparing the time averaged velocity profiles observed with different inflow rates; (a) Inflow rate = 0.75 L·min^{-1}; (b) Inflow rate = 1.00 L·min^{-1}; (c) Inflow rate = 1.25 L·min^{-1}; 39
6.8 Time averaged velocity of fluid over a straight line on xz plane located at the taphole height. 39
6.9 Time averaged void fraction of the bed for different flow rates; (a) Inflow rate = 0.75 L·min^{-1}; (b) Inflow rate = 1.00 L·min^{-1}; (c) Inflow rate = 1.25 L·min^{-1}; . . 40
6.10 Verification of solid - fluid heat transfer code with analytical solution; The temperature profile of solid phase with time. 42
6.11 Comparing the temperature of solids in experimental results of Messai et al. and the CFD-DEM model results over time [7]. 43
6.12 Comparing the results of air temperature as predicted by the model and the analytical solution of Yagi et al. (1959). 45
6.13 (a)Temperature profile of the simulation with wall-particle heat transfer;(b)Temperature profile of the simulation with wall-particle heat transfer;(c)Comparing the results of axial temperature profiles with and without wall-particle heat transfer. 46
6.14 (a) Verification of solid to fluid mass transfer accompanied by convected mass transfer with analytical solution. (b) Axial and radial concentration profile of a system with water flowing through a bed of benzoic acid spherical packing. 48
6.15 Verification of particle size reduction in the model with the analytical solution. . . 48
6.16 (a) Volume fraction of the fluids, water and air in the system to check for the mass transfer at the interface via diffusion; (b) Concentration profile in the column at the end of 20s; The saturation concentration in the system is illustrated to assess the concentration profile; The red dotted line represents the interface. 49

List of Tables

3.1 Properties of fluids and solids in furnace compared to setup [8] 12
3.2 Properties of the magnetic tracking particle used for the experiments 16
3.3 Parameters used during experiments to determine the influence of inflow rates on bed dynamics 16

5.1 Values for parameters selected for optimising the PID control and burden plate movement with the bed. 28
5.2 Net migration of particle in the bed as a result of different inflow rates of water. . 30

6.1 Properties and parameters of fluid and solid phases for evaluating the influence of fluid inflow rates on bed dynamics. 34
6.2 Properties and parameters of fluids and solids for verification of heat transfer model. 41
6.3 Properties and parameters of fluids and solids for verification of heat transfer model in a non adiabatic packed bed. 44
6.4 Comparison of heat flux calculated by the model with manual calculations. 45
6.5 Properties and parameters of fluid and solid phases for verifying the mass transfer model. 47
6.6 Properties and parameters of fluid and solid phases for evaluating the mass transfer at the interface. 49

Chapter 1

Introduction

1.1 Iron and Steel Industry

With the global economic growth, the global production of iron and steel has increased rapidly over the years. Figure 1.1 shows the increased rate in production of iron and steel over the last few decades [1]. The year 2018 alone witnessed 1808 million tons of iron globally [1]. Production rate in the last 60 years (i.e. 189 million tons in 1950 to 1808 million tons in 2018 globally) stacks up to a ten fold increase.

Hence, to meet the demands of the development, industries are continuing to optimize the production of iron and steel and setting up more production sites. Steel making process is currently divided between the oxygen steel making and electric steel making process. The former uses iron ore as raw mater and a blast furnace for the production while the latter utilises an electric arc furnace with scrap metal as raw materials. Most of the steel and iron is currently produced through the oxygen steel making process using a blast furnace [1]. The products from these furnaces are then refined to obtain the finished steel products via numerous downstream processes. With better understanding of the above processes, the production of iron and steel can be optimized to achieve higher efficiencies. This work mainly focuses on the former process where a blast furnace is used.

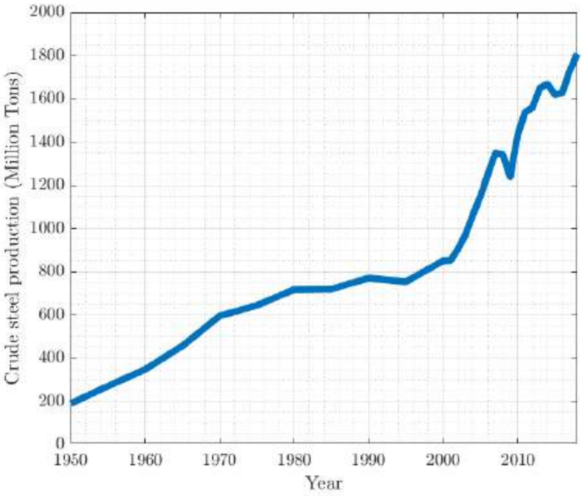

Figure 1.1: Global crude steel production over the years [1]

1.2 Blast Furnace

The blast furnace is a large counter current reactor with diameter ranging from 10 to 15m and up to 40m tall [9].The temperatures in the blast furnace vary in the range of 200°C to 2100°C (figure 1.2) [9].

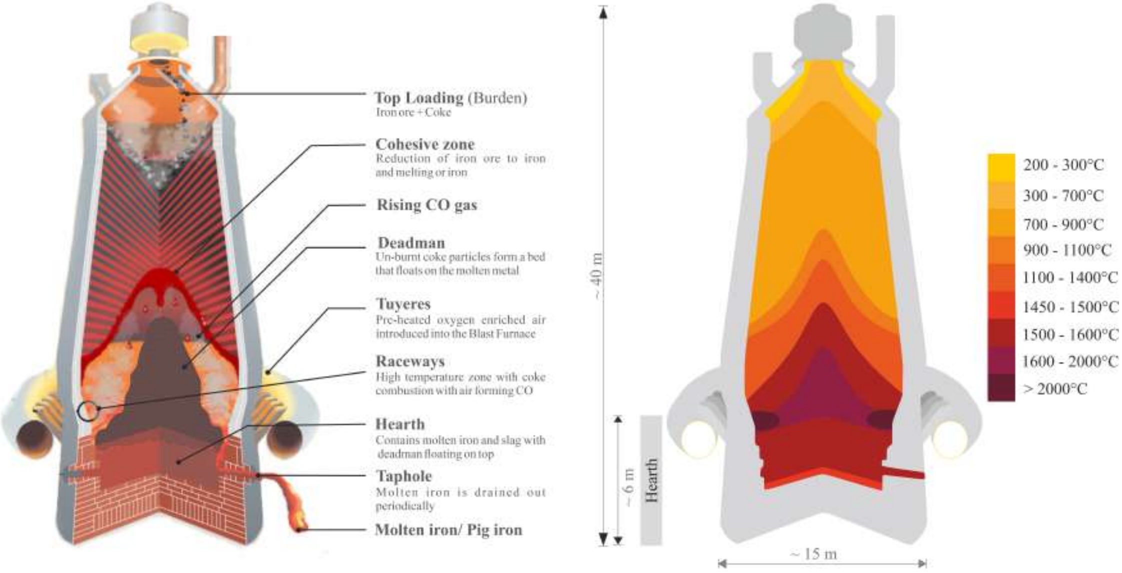
Top Loading (Burden)
Iron ore + Coke
Cohesive zone
Reduction of iron ore to iron and melting or iron
Rising CO gas
Deadman
Un-burnt coke particles form a bed that floats on the molten metal
Tuyeres
Pre-heated oxygen enriched air introduced into the Blast Furnace
Raceways
High temperature zone with coke combustion with air forming CO
Hearth
Contains molten iron and slag with deadman floating on top
Taphole
Molten iron is drained out periodically
Molten iron/ Pig iron
~ 40 m
~ 6 m
Hearth
~ 15 m
200 - 300°C
300 - 700°C
700 - 900°C
900 - 1100°C
1100 - 1400°C
1450 - 1500°C
1500 - 1600°C
1600 - 2000°C
> 2000°C

Figure 1.2: Blast furnace Cross section with zones and temperatures

The raw materials for the blast furnace constitute iron ore (oxides of iron), coke (carbon rich lumps) and oxygen enriched air. The ore and the coke particles are loaded from the top while pre-heated enriched air enters from the bottom through tuyeres. The enriched air reacts with the coke to form carbon monoxide (CO) as represented in equation 1.1. CO reduces the iron oxides in a series of reactions producing carbon dioxide (CO_2) and iron as shown in equations 1.2-1.6. In addition, the process of coke oxidation is exothermic and the heat produced aids in melting the newly formed iron. The liquid iron drips to the hearth of the furnace before being tapped at the bottom.

$$\mathrm{O_2 + 2\,C \longrightarrow 2\,CO} \tag{1.1}$$

$$\text{Hematite :} \quad \mathrm{3\,Fe_2O_3 + CO \longrightarrow 2\,Fe_3O_4 + CO_2} \tag{1.2}$$

$$\text{Magnetite :} \quad \mathrm{Fe_3O_4 + CO \longrightarrow 3\,FeO + CO_2} \tag{1.3}$$

$$\text{Wustite :} \quad \mathrm{2\,FeO + CO \longrightarrow 2\,FeO_{0.5} + CO_2} \tag{1.4}$$

$$\mathrm{2\,FeO_{0.5} + C \longrightarrow 2\,Fe + CO} \tag{1.5}$$

$$\mathrm{CO_2 + C \longrightarrow 2\,CO} \tag{1.6}$$

The iron ore used in blast furnaces commonly are in the form of sinters ($dp < 25$)mm, pellets ($dp \sim 11 \pm 2$)mm or lumps (dp $6 - 25$)mm [10]. The coke particles and the ore is added from the top in alternating layers for optimum permeability of reduction gases as the metal melts. The enriched air react with the coke forming large cavities next to the tuyeres called raceways, with temperatures reaching 2100°C as illustrated in figure 1.2. The reduction gas i.e. carbon monoxide moves up the blast furnace reducing the iron oxides and providing heat to melt the iron that is formed. The coke particles remain solid while the iron melts. The molten iron trickles down a bed of coke particles. This section is referred to as the cohesive zone which is found just above the raceways. The impurities in ore such as silicon dioxide and other metal oxides separate from the iron ore at high temperatures forming a glassy liquid termed slag.

The molten metal with the slag flow into the bottom section of the furnace titled the hearth. The solid coke particles with lower density float on top the slag and molten metal. This creates a bed of carbon particles on top of the hearth while the combustion and high pressures at the raceways impart a conical from to the bed. This bed is often termed the deadman as shown in figure 1.2. Finally, the molten metal is tapped from the hearth by drilling holes into the walls of the furnace.

The walls of the blast furnace hearth are constantly under stress due to the high temperatures and viscous flow of the molten metal and slag during tapping. The repairs to the walls or relining of the hearth are found to be more difficult and expensive when compared to other parts of the furnace. The campaign life of a blast furnace is highly dependent on the durability of the hearth [11]. Hence, this project is aimed at understanding the dynamics of the hearth region of the blast furnace.

1.2.1 Hearth and Deadman

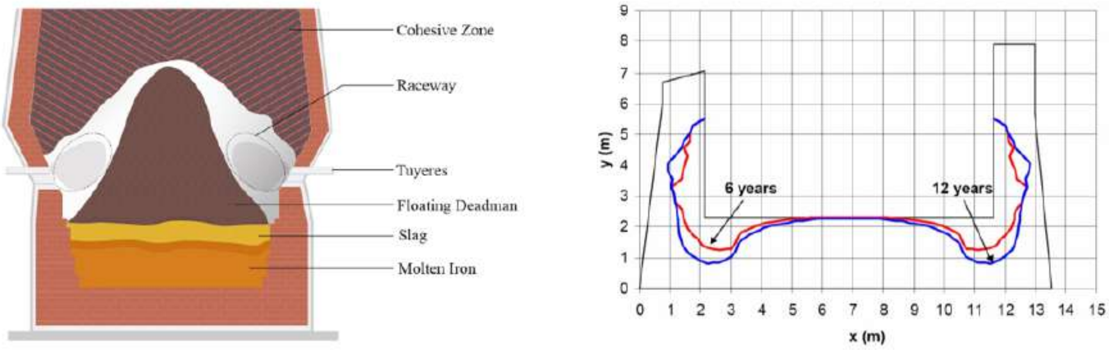

Figure 1.3: (a) Hearth section of the blast furnace; (b) “Elephant foot” corrosion profile for a carbon based crucible [2]

The hearth is filled with molten metal, with slag floating on top. The heat and flow of molten metal apply constant stress on the walls of the hearth. Further, the deadman floating on top of the hearth section applies force on the metal and hinders free flow of the molten metal. It is often observed that the molten iron flows around the deadman with higher velocity. This essentially forms a circumferential flow in the hearth resulting in higher stress on the walls of the hearth [12]. Over time, it has been observed that higher velocities at the circumference erodes the walls (as seen in fig.1.3) forming a shape commonly referred to as the *“elephant’s foot”* [13].

Further, it has been observed that carbon has high affinity towards molten iron. The walls and linings of the hearth are usually made of carbon ceramic composites to withstand the heat. Adversely, the carbon from the walls slowly dissolve into the metal resulting in further erosion over time.

There have been numerous attempts at understanding the dynamics of blast furnace and the hearth over the years. Early attempts include onsite studies of blast furnace where observations were made based on molten metal outflow data and dig-outs [3][10]. The constraints of high temperature and enormity of the structure limit the opportunities of understanding the dynamics inside a blast furnace as onsite measurements are complex. Further, the high temperatures in the blast furnace make it quite difficult to obtain more dynamic data on metal flow, influence of deadman, stress on the walls and rate of heat and mass transfers inside. Hence, an alternate idea of representing a blast furnace as a mathematical model to understand the dynamics has gained popularity in the recent years. [4]. Later attempts include the development of models representing the furnace [4][14][5]. These methods are discussed in detail in the upcoming second chapter.

This project was designed at understanding the dynamics of blast furnace hearth where the main focus is towards the molten metal flow, deadman dynamics accounting the effects of heat and mass transfer between the phases.

1.3 Subject of Research

The hearth of the blast furnace determines the efficiency and campaign life of the furnace. The hearth is also home to complex multiphase heat and mass transfer phenomena. These facts make the blast furnace hearth a highly relevant research topic. The focus of this project is on:

1. Conducting experiments to determine the influence of inlet flows on bed dynamics. In addition, performing simulations with experimental data for further analysis.
2. Modelling the heat transfer in a packed bed based on CFD-DEM coupling.
3. Modelling the mass transport in a packed with particle dissolution.

Chapter 2

Literature Survey

2.1 Early attempts at understanding Dynamics of Blast Furnace

The operation of blast furnace involving molten metal,temperatures up to 2100°C and corrosive gases creates a hurdle for physically gathering data on blast furnace internals [15]. Therefore, most of the onsite data is indirectly procured i.e observations pertained to the inlet and the outlet of the blast furnace. These observations provide useful information on the working of the furnace but, most often a complete understanding of the furnace dynamics may not be derived from them.

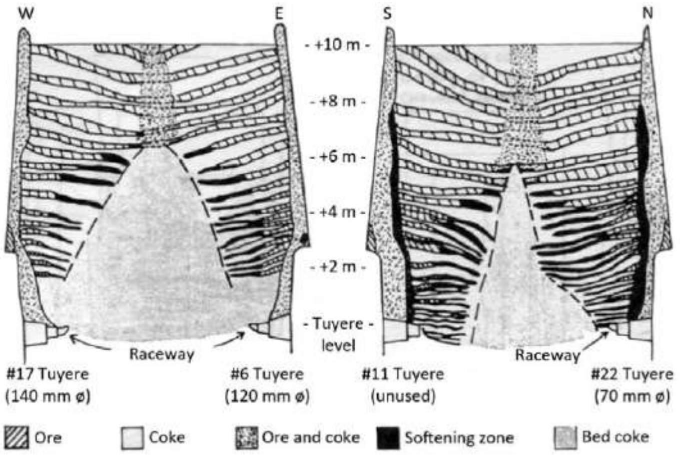

Figure 2.1: Dig-out of the Kokura 2 Blast Furnace [3]

Early methods to understand the insides of a blast furnace was with quenching and digging the blast furnace to obtain a cross section for visualization. Blast furnace No. 2 at Sumitomo Metals Corporation Kokura, Japan (1974) [3] (figure 2.1) was quenched with water while Blast Furnace No. 5 at Mannesmannröhren-Werke (1981) and a British Steel experimental furnace were quenched with liquid nitrogen [16]. The furnaces were then drilled to visualize and obtain insights on the workings of blast furnace. This provided useful information on the burden and the cohesive zone in the blast furnace. Unfortunately, the data on hearth and deadman were limited. Furthermore, the method was restricted to decommissioned furnaces and provided little information on dynamics of the process.

2.2 Mathematical model of Iron making process

2.2.1 Four-Fluid Model of Blast Furnace

Over the years, approaches at mathematically modelling the blast furnace to understand the dynamics gained popularity. Models of the blast furnace hearth have been developed using the continuum method with blast furnace considered to be a moving packed bed since early 1980 [17]. Results of the model provide dynamic data on the process and are comparatively economic as they do not intervene with the onsite production. Yagi et al. (1993) has written an extensive review on the work done in which the packed bed is modelled as comprising four fluids i.e. gas, liquid, solid particles and fine powder (see figure 2.2) [4]. The flow is modelled by the generalized equations for continuity and the Navier-Stokes equations for motion. As this is a continuum approach based on local averaging, the four fluids are defined by the respective volume fractions.

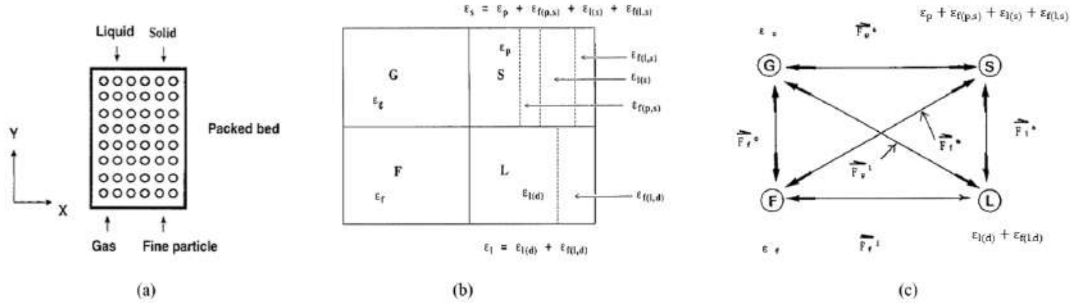

Figure 2.2: (a) Representation of the four fluids in the packed bed; (b) Phase fractions in the bed with G - Gas, S - Solid, F - Fine powder, L - Liquid; (c) Interactions between the phases of the model [4].

The four fluid model was adopted for further predictions on reaction kinetics, heat and mass transfer. These adaptations also improved the model with better assumptions and fewer predefined or assumed parameters. Austin et al. (1997) built on the four fluid model introducing heat transfer and reactions [18]. De Castro et al. (2000) considered hot metal and slag as separate fluids in the blast furnace hearth [19]. Zaimi et al. (2000) adapted the model to predict the deadman dynamics rather than predefining it unlike the earlier cases [20]. Chew et al. (2001) incorporated the heat transfer and reactions between gases, liquid and solids [21].

The increase in computation power over the years provided the advantage of modelling the particles as discrete entities over continuum approximations as before. Hence, more of the models adapted discrete methods of modelling for particles while treating fluids as a continuum.

2.2.2 CFD-DEM model of Blast Furnace

Zhou et al. (2008) presented a 2D model which combined the solid particle behaviour and fluid flow. The model used Discrete Element Method (DEM) to simulate the particle movement while fluid flow was modelled with Computational Fluid Dynamics (CFD) [22]. This method gained popularity where solids are treated discretely rather than being allegorized as a continuum.

The ideology of Discrete Element Method was developed by Cundall and Strack in 1979 where motion of the particle is tracked using contact forces and Newton's second law of motion [23][24]. DEM and CFD are coupled by the momentum and energy exchange between the solids and the fluid.

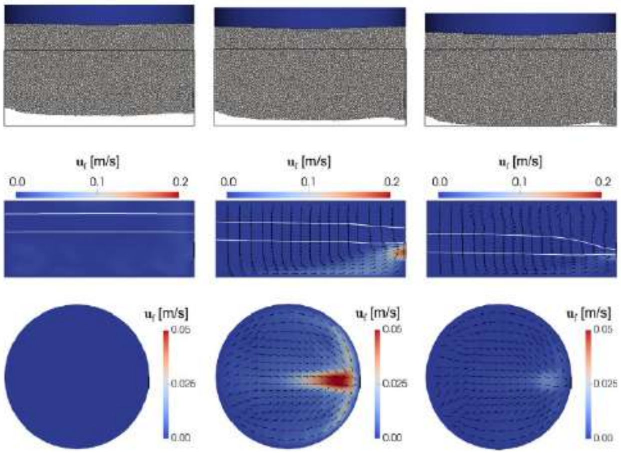

Figure 2.3: Snapshots of the blast furnace hearth at three different times. The columns represent from left to right t = 0 s , t = 5 s and t = 20 s . The first row shows the deadman and the force walls, the second and the third row depicts the velocity field at Plane y and Plane z respectively. The white lines visualize the air-slag (upper) and iron-slag (lower) interfaces. [5]

An open source system, CFDEM® was developed by Kloss, Goniva and others [25][26][27]. CFDEM® has been adapted by many to describe the dynamics of blast furnaces. Adema et al. (2009) developed a blast furnace model using the CFD-DEM coupling approach to investigate the cohesive zone [14]. The results obtained included the discrete treatment of particles for the dynamics in the cohesive and burden zones of the blast furnace. This procedure was also adopted by Natsui et al. (2011) to investigate the unbalanced gas flow in the lower part of the blast furnace [28]. Vangö et al. (2017) further utilized an unresolved approach of CFD-DEM to investigate the process of tapping [29]. The results were promising as the carbon particles of deadman were dynamic and involved particle collisions. CFD-DEM was successfully used to model the raceway patterns in the works of Miao et al. (2017) [30]. Bambauer et al. (2018) provided a model to analyse the transient solid and fluid flows with stress distribution on walls [31]. Wei et al. (2019) further investigated the heat transfer at raceways using ellipsoidal particles [32].

2.3 Heat transfer

The hearth functions as a packed bed as mentioned earlier where deadman makes the bed of particles while molten iron forms the fluid. Hence the dynamics of a packed bed can be extended to the hearth [29].
The heat transfer paths in a packed bed (here, the hearth) can be broken down as

- Heat transfer between the solid coke particles
- Heat transfer between the coke particles
- Heat transfer between the bed and walls of the furnace
- Conduction through the molten iron

The heat transfer between the particles in contact have been modelled based on the area of contact. Chaudhuri et al.(2006) proposed a method to calculate the heat transferred between two particles in contact [33]. The area of contact was first calculated based on the normal force and Young's modulus. The heat transferred was calculated with this area of contact, effective thermal conductivity and the temperature gradient. The model by Chaudhuri et al. considered just the heat conduction between the two particles while the models proposed by Bu et al. (2013) [34] and

Tsotsas et al. (2019) [35] also considered the heat transfer through the fluid film and fluid gaps between the particles.

The heat transfer between the particles of the packed bed and the fluid flowing through it are relatively well established with empirical formulae. Few of the proposed methods are by Ranz and Marshall (1952), Williams (1942) or Whitaker (1972) [36]. Gunn (1978) proposed an equation which correlated the Nusselt number with the Prandtl and Reynolds numbers [37].

The conduction through the fluid is affected by the irregular particle distribution in the cross section. The most effective method to evaluate the heat transfer in the cross section is by obtaining an effective heat transfer coefficient. This effective coefficient accounts for both particle and fluid heat transfer. This idea has been adopted by several researchers and there are different methods to calculate the effective thermal conductivity of the fluid. Yagi and Kunii (1957) conducted experiments with a packed bed and proposed an empirical formula for the effective coefficient based on Reynolds, Prandtl numbers and void fractions [38]. The formula was relies on the particle to tube diameter ratio. Similar formulae were proposed by Yagi and Wakao (1959), Wakao and Kato (1969) which allowed for a broader particle to tube diameter ratio [39] [40].

$$\frac{k_e}{k_f} = 6.0 + 0.11 Pr Re_p \qquad for \qquad \frac{D_p}{D_T} = 0.021 \sim 0.072 \tag{2.1}$$

$$\frac{k_e}{k_f} = 6.0 + 0.09 Pr Re_p \qquad for \qquad \frac{D_p}{D_T} = 0.12 \sim 0.17 \tag{2.2}$$

The methods proposed by Yagi and others were largely material dependent, sometimes limited by diameter ratios and empirical coefficients as shown in equations 2.1 and 2.2. Zehner and Schlünder (1970) proposed a method to calculate effective thermal conductivity which was less dependent on experimental findings and hence was applicable to larger applications [41]. The approach was widely accepted and modified by many to account for different parameters which were assumed or neglected previously [42]. Bauer and Schlünder (1978) revised the correlation to account for the radiation and this is commonly known as ZBS correlation for the names of the authors [43]. It calculates the effective thermal conductivity based on the individual conductivity of the phases, void fraction. The ZBS equation has been accepted widely and has been modified slightly for different applications since [44] [45].

The heat transfer near the walls in a packed bed is significantly different from the bulk of the system. This is explained by the boundary layer of fluid at the walls and relatively high void fractions near the wall [46]. Yagi and Kunii (1960) proposed a method to calculate the rate of heat transfer at the walls [47]. The heat transfer at the walls was interpreted in term of the J-factor introduced by Colburn. It was calculated based on the particle Reynolds number [39]. Dixon et al. (1988) demonstrated the particle shape effects on wall heat transfer [48].

Heat transfer in Blast Furnace Hearth

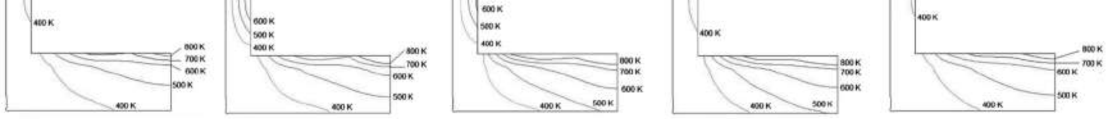

Figure 2.4: Calculated predictions of temperature profiles in the BF hearth walls. [6]

The heat produced by the combustion of coke in the raceways melt the iron which drips into the hearth through the cohesive zone and the deadman [32]. The high temperatures and molten iron in the hearth contribute immensely to wear of the walls of the hearth [49]. Gdula et al. (1985) analysed the steady state heat transfer in hearth with a mathematical model [50]. The work of Kumar et al. (2005) provided more data on the heat transfers in the hearth and its impacts on refractory (lining of the walls) wear [49]. The different pathways for heat transfer in a blast furnace hearth was analysed by Zhang et al. (2008) [51]. Swartling et al. (2010) reported the findings of the heat transfer between the walls and bed based on Blast furnace No.2 at SSAB Oxelösund, Sweden [6] (figure 2.4). A 2D model was developed by Kumar et al. (2018) which predicted the heat transfer in the hearth of the blast furnace [52]. The analysis was performed with more importance towards the fluid while the heat transfer between solids was of minor interest.

2.4 Mass Transfer

The hearth section of the blast furnace consists of molten metal, slag and the solid coke particles of deadman. The carbon has affinity towards the molten iron resulting in the dissolution of coke particles in the fluid phase. The walls of the blast furnace is lined with high temperature refractory materials to contain and withstand the molten metal between tapping cycles. To achieve high temperature resistance the refractory materials are usually made of carbon ceramic composites. The carbon from these linings also dissolves into the molten metal. While this happens at low rates, it is found to be significant over the years [53]. This causes wear in the wall linings which is undesirable. There have been numerous studies regarding refractory lining wear in the blast furnace over the years. Silva et al. (2005) and Jiao et al. (2016) provide a detailed analysis of hearth wall wear mechanisms and protective layer formation (skull layer) [12][54]. Takatani et al. (2001) developed a model that describes and predicts the process of wear in the walls [55]. Post et al. (2003) studied the mass transfer and dissolution of coke particles in molten metal.

To predict the carbon transfer from the coke particles, experiments were conducted to obtain the parameters that define the mass transfer. Gudenau et al. (1990) conducted experiments at 1550°C where the rate of dissolution of carbon in molten iron was determined [56]. The rate of mass transfer was established as a function of fluid flow around the solid carbon. It was also observed that the mass transfer of carbon from the particles to fluid was often hindered by the ash formation on the carbon surface. The correlation accounted for this ash layer formation as well (equation 2.3). Jones (1998) looked into the kinetics of carbon dissolution in molten iron where he summarized the saturation concentration of carbon in molten iron as a function of temperature 2.4. Jones also summarized the effect of temperature on physical properties of molten iron.

$$k = k_0(u)^{0.7} \cdot exp\left(-k_0(u)^{0.7}\frac{A_p}{V_m}t\right) \tag{2.3}$$

$$C_s = \frac{1.34 + (2.54 \cdot 10^{-3})}{100}(T_f - 273.15) \tag{2.4}$$

where $k_0 = 0.00211$, u is the velocity of the fluid, A_p is the interfacial surface area of the coke particle and t is the time and T_f is the temperature of molten iron.

With the above correlations, Post et al. (2003) and Reuter et al. (2005) developed a simple 2D and 3D model for analysing mass transfer in blast furnace hearth [57][58]. The effects on density changes of the hot metal due to carbon dissolution was studied. Carbon dissolution from refractory bricks, refractory wear was evaluated by analysing fluid flow along the wall. The effects of coke properties such as dissolution or mass transfer rate constants on hot metal flow were analysed.

Chapter 3

Methodology - Experimental

The experimental work aims to investigate the flow and bed dynamics of the blast furnace hearth at a small scale. Further, this work is aimed at assessing the impact of inlet flow rate on the dynamics of the packed bed. The data from experimentation is later used to validate the pre-developed numerical model. The setup is designed to perform cold experiments with water substituting the molten metal and alumina shells representing the coke particles of the deadman (section 3.1 . The setup is designed to include the features of blast furnace such as tapholes, raceways and burden forces that are perceived to play a key role in bed dynamics. The system consists of continuous, constant inflow of water while the tapholes are automated to be opened and closed as desired. In addition, Magnetic Particle Tracking (MPT), a non-invasive or non-destructive method is used to monitor the particle movement inside the setup. This allows for a nearly complete study of the particle and bed dynamics of the setup.

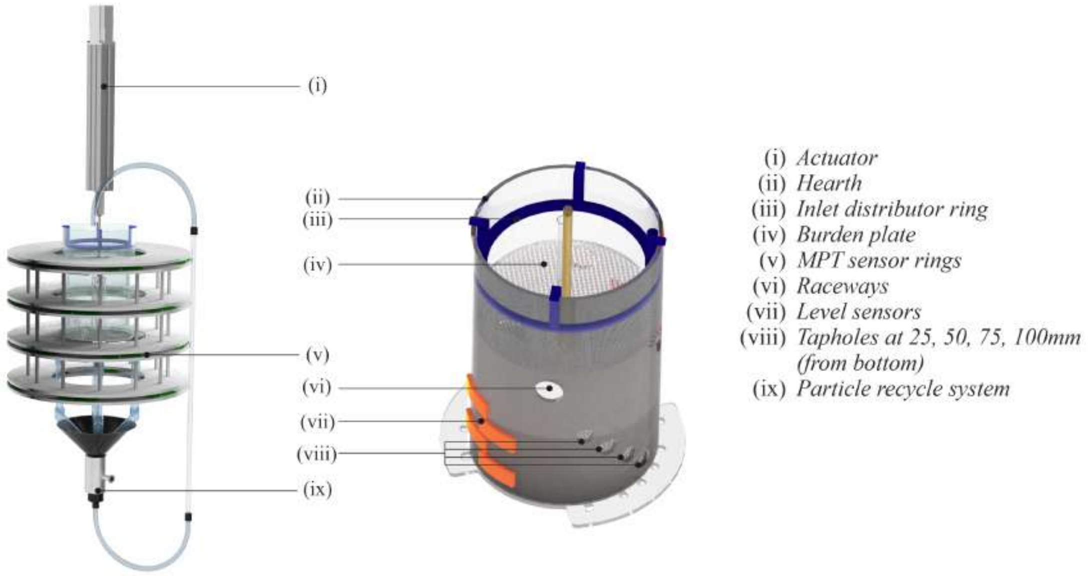
(i)
(ii)
(iii)
(iv)
(v)
(vi)
(vii)
(viii)
(ix)
(i) Actuator
(ii) Hearth
(iii) Inlet distributor ring
(iv) Burden plate
(v) MPT sensor rings
(vi) Raceways
(vii) Level sensors
(viii) Tapholes at 25, 50, 75, 100mm (from bottom)
(ix) Particle recycle system

Figure 3.1: (a)Experimental setup of the hearth with MPT system and different components.

3.1 Material Properties

The idea of using water to represent molten iron flow is a common practice in cold experiments [5][57]. This can be justified as the kinematic viscosity of the two are similar. The alumina shells are chosen as they are less dense than water and possess good structural strength. The latter of the properties help the shells stay intact during the collisions and recycle. The properties of the fluids and solids in a blast furnace is compared to the set up in table 3.1.

Table 3.1: Properties of fluids and solids in furnace compared to setup [8]

	Molten Iron (1550 °C)	**Coke Particle**	**Water** (25 °C)	**Alumina Shells**
ρ $[kgm^{-3}]$	6998	∼900	997.07	405
ν $[m^2s^{-1}]$	8.09×10^{-7}	-	8.93×10^{-7}	-
	Blast Furnace		**Experimental set up**	
ρ_p/ρ_f [-]	0.1286		0.4061	

3.2 Experimental Setup

3.2.1 Hearth

A ploycarbonate cylinder is used for the construction of cold furnace hearth. The diameter to height ratio of the cylinder is similar to a large scale blast furnace hearth. The system consists of multiple tapholes placed at varying heights from the base. This allowed Hoeks (2019) to investigate the influence of relative taphole heights on bed dynamics.

3.2.2 Deadman

The particle size plays a key role in dynamics of the moving packed bed. The particle size used for experiments were decided based on particle Reynolds number observed in blast furnaces. This resulted in particle size of approximately 5 mm diameter for the experimental setup.

Further, the particles were coated with a hydrophobic nanocoating solution to reduce surface tension with water. This aids in avoiding particle agglomeration during particle recycle. The particles were sorted to obtain the particle size in the range of 4.5 - 5.6mm (d_p). The particle size distribution is shown in figure 3.2 depicting the size before and after sorting.

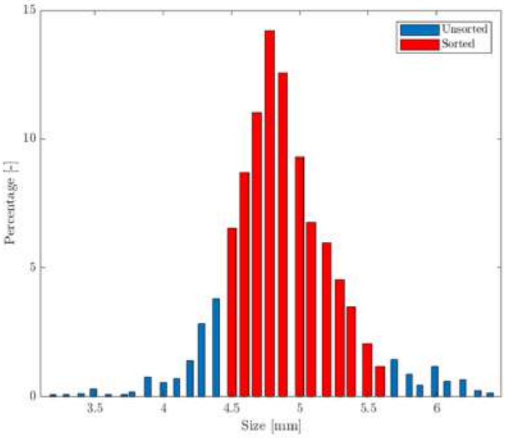

Figure 3.2: Particle size distribution

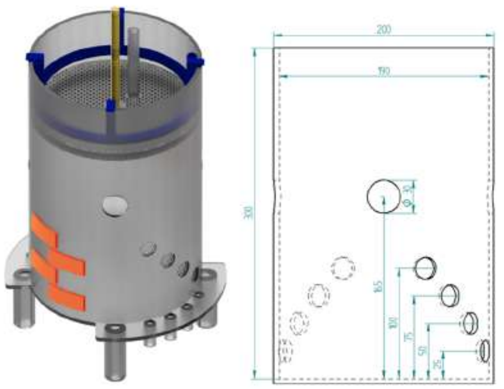

Figure 3.3: Vessel representing the hearth

3.2.3 Fluid flow

The water flow is introduced into the setup by a distributor ring which splits the flow in four and directs the flow towards the vessel wall. This is to ensure equal flow through the circumference (figure 3.4 (b)). Additionally, the design avoids the water from entering the exit windows designed to represent the raceways. The system is equipped with a flow controlled pump to set the desired inflow rates.

The water is drained through tapholes located at different heights in the bottom section of the cylinder. The tapholes are separated by a distance of 25mm axially and arranged on a diagonal line inclined at 15°with the base (figure 3.3). The valves for the tapholes are automated for scheduled outflow of water. Flow sensors are used to record the outflow rates of the water. Further, the tapholes are designed with perforated entrance to avoid exit of particles.

The water is drained from the setup freely under the influence of gravity. Five level sensors are attached to the cylinder just above the tapholes and one just below the raceway (orange blocks in figure 3.3). Level sensors detect the water level inside the system and are used as switches to operate the tapholes. As the water level approaches the raceway, the taphole is opened to drain the water from the system. The taphole is then closed when the water level reaches the height of the taphole. Throughout this process there is a constant inflow of water that results in the rise and fall of the water and floating bed. This mimics the periodic tapping cycles observed in the blast furnace operation.

3.2.4 Burden Force

In a blast furnace, the deadman is subjected to constant downward force from the cohesive zones and the burden loaded on top. The force applied by the burden plays a key role in the dynamics of the deadman. Hence, it is essential to introduce this force in the setup for a complete study.

The setup is designed to accounts for this force through a perforated plate attached to a linear actuator (figure 3.4 (c)). This plate applies a force to the particle bed without blocking the liquid flow. A force sensor is installed in the actuator shaft and a PID controller is used to keep the applied force constant throughout the tapping cycles.

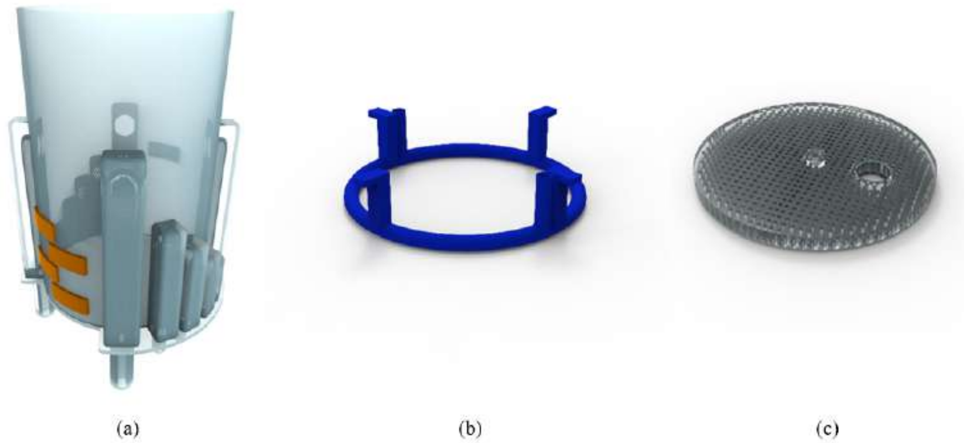

Figure 3.4: (a) Cylindrical vessel representing the hearth and tapholes (b) Inlet route for the water (c) Burden plate that applies force on the bed.

3.2.5 Raceway and Particle Recycle

The raceways in a blast furnace are found behind the tuyeres on the top of the hearth. The coke particles undergo combustion at the raceways. This area is highly turbulent and the gas velocity in this region is very high, pushing the rest of the bed inwards providing the characteristic cone shape for the deadman.

Since the combustion in raceways essentially removes the solids from the system, the same approach has been followed in the setup. The raceways are represented as exit holes located above the tapholes. These exit holes are located on the walls in each quadrant of the cylindrical vessel at a height of 165mm from the bottom. The particles rise with the water level and as they reach the height of raceways, particles next to the raceways fall through these apertures and exit the system. As the particles close to the raceways are removed, the height of the bed at the center is greater than the height at the circumference. This allows for the particle bed to reshape as a conical structure as observed in the blast furnace deadman.

In a blast furnace, particles are continuously supplied to the deadman from above. The setup mimics the same through the process of recycle. The particles that exit the system through the raceways are recycled via pneumatic conveying and added to the top of the bed. An optical gate records the number of particles being recycled in the system.

With the inclusion of the above operations, the setup is enabled to represent most of the important aspects of the blast furnace that allows us to study the flow and bed dynamics as a whole.

3.3 Particle Dynamics

3.3.1 Bed movement

The dynamics of the bed is influenced by various parameters in the system. The bed is initially resting on the bottom of the hearth. As the fluid starts flowing through the bed of particles, it gets collected around the bed. The fluid now applies a buoyant force on the bed pushing it up and the bed starts to float. The burden plate from the top applies force on the bed pushing the particles down into the fluid. The downward force from the burden plate is less than the upward buoyant force; hence, the bed continues to floats in the fluid. When the taphole is opened, the fluid is drained from the system, the net buoyant force decreases and the bed returns to rest on the bottom of the hearth. This process repeats again when the taphole is closed and volume of fluid increases in the system. With the tapping cycles, the bed attains a periodic upward and downward motion. Further, during these movements, the particles at the wall additionally experience friction with the wall. Therefore, the force experienced by a particle at the wall is different from the force experienced by a particle in the bulk of the bed.

To observe the particle movement, Magnetic Particle Tracking (MPT) has been employed in this work.

3.3.2 Magnetic Particle Tracking

Magnetic Particle Tracking (MPT) is a non invasive technique that uses a magnetic marker to track a single tracer over time. The setup consists of multiple sensors arranged around the system , detecting the magnetic field generated by the tracer particle. The data from these sensors are processed to obtain the particle position and a trajectory of the particle over time.

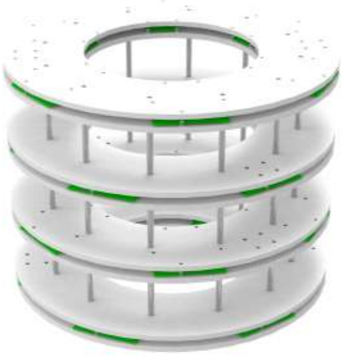

Figure 3.5: Magnetic Particle Tracking system with a total of 72 sensors split over 4 discs.

MPT is one of the many non invasive techniques like RPT (Radioactive Particle Techniques), PEPT (Positron Emission Particle Tracking) or PTV (Particle Tracking Velocimetry). MPT uses a magnetic tracer particle and therefore is a safer method compared to few other methods that involve radioactive tracers. MPT is also suitable for full 3D systems, unlike PTV, which is limited to pseudo 2D system. Furthermore, MPT possess the advantage of tracking a the tracers position as well as its orientation [59].

Working Principle

Buist et al.(2014) developed an algorithm for analysing the data from the sensors to track a magnetic particle. The analysis of MPT data is based on the quasi-state field around the magnetic marker. The evaluation of the quasi static magnetic field provides estimates on the particle positions.

Assuming a position of a tracer with a known magnetic moment, the magnetic field ($\vec{H}$) generated by it is given by equation 3.1.

$$\vec{H}(\vec{e}_p, \vec{r}_{ps}) = \frac{1}{4\pi}\left(-\frac{\mu_m \vec{e}_p}{|\vec{r}_{ps}|^3} + \frac{3\mu_m(\vec{e}_p \cdot \vec{r}_{ps})\vec{r}_{ps}}{|\vec{r}_{ps}|^5}\right) \tag{3.1}$$

With $\vec{r}_{ps} = \vec{r}_p - \vec{r}_s$.

The calculated magnetic field ($\vec{H}$) is used to obtain the theoretical signal strength (S_t). This theoretical signal strength is compared to the actual measured signals to obtain the quality function (equation 3.3). Consecutive new values for the position and orientation are obtained to minimise Q. Once the quality is below the predefined threshold (value), the tracer position and orientation have been obtained.

$$S_t = \vec{H}(\vec{e}_p, \vec{r}_{ps}) \cdot \vec{r}_s \tag{3.2}$$

$$Q = \sum_{i=1}^{72} \frac{((S_{m,i} - \langle S_m \rangle) - (S_{t,i} - \langle S_t \rangle))^2}{\Delta S_{m,i}^2} \tag{3.3}$$

In our setup, a total of 72 Anisotropic Magneto-Resistive (AMR) sensors are split between 4 discs along the circumference of the hearth (figure 3.5). The four discs are separated by a distance of 150mm. The sampling frequency was set to 50Hz during the measurements. Further, the whole setup was placed inside a Helmholtz coil to correct for the magnetic fields of the earth (figure 3.1 (a)).

In the experiments, the tracer used was a particle with a diameter of 6mm, density while the magnetic moment of the tracer was 0.0304 A·m^2.

Table 3.2: Properties of the magnetic tracking particle used for the experiments

Property	**Value**	**Units**
Magnetic moment (μ)	0.0304	[A·m^2]
Diameter	6	[mm]
Density	890	[kgm^{-3}]

3.4 Flow Experiments

Three inflow rates, 0.75, 1.0 and 1.25L·min^{-1} were selected for experiments. The flow rates were opted such that the flow of fluid into the system was lower than the maximum outflow. With a constant inflow of the fluid and periodic drainage of the system, a cyclic rise and fall of fluid in the system was achieved. The hearth was filled with particles to a height of 120mm. With an irregular packing of the particles, the number of particles in the system was calculated to be about 33·10^3. A magnetic tracer particle is placed between the particles at the top of the bed to track its movement. A force of 2N is applied on the bed of particles through the burden plate.

Experiments were conducted for 900s. Runs were performed for every inflow rate twice, to check for any irregularities in the system.

Table 3.3: Parameters used during experiments to determine the influence of inflow rates on bed dynamics

Parameter	**Value**	**Units**
Inflow rates	0.75 / 1.00 / 1.25	[L·min^{-1}]
Burden force	2	[N]
Taphole height	0.025	[m]
Upper switch point	0.1	[m]
Lower switch point	0.25	[m]
Number of particles	~33000	[-]

The magnetic tracking system records the particle position over time in 3D space. The inflow rate, burden force were monitored to check for the system operations. The outflow rates were recorded with the periodic operation of the taphole valves.

Chapter 4

Methodology - Modelling

CFDEMCoupling software is utilised to simulate a moving packed bed. This relies on LIGGGHTS® to model the particle dynamics through Discrete Element Method. Additionally, OpenFOAM® libraries are utilised to solve volume-averaged Navier-Stokes equation to evaluate the fluid flow. CFDEM® performs a two way coupling to analyse the interaction between the fluid and the solids.

4.1 Computational Fluid Dynamics

Computational Fluid Dynamics (CFD) is a class of numerical tools widely used to simulate and evaluate fluid flow. In the finite volume method, the geometry is divided into smaller units. The PDEs describing the fluid flow are discretised on these cells, taking into account the their boundary conditions. The governing equations are represented as

Continuity Equations:

$$\frac{\partial \varepsilon_f}{\partial t} + \nabla \cdot (\varepsilon_f \vec{u}) = 0 \tag{4.1}$$

Navier-Stokes Equation:

$$\begin{aligned} \frac{\partial \varepsilon_f \rho_f \vec{u}}{\partial t} + \nabla \cdot (\varepsilon_f \rho_f \vec{u}\vec{u}) = -\varepsilon_f \nabla p + \nabla \cdot (\varepsilon_f \overline{\overline{\tau}}) + \rho_f \varepsilon_f g - \vec{F}_{pf} \\ with \qquad \overline{\overline{\tau}} = \mu_f \left[(\nabla \vec{u}) + (\nabla \vec{u})^T \right] \\ \vec{F}_{pf} = \frac{1}{\Delta V} \sum_{i=1}^{n} (\vec{f}_{d,i} + \vec{f}_{l,i} + \vec{f}_{vm,i} + \vec{f}_{B,i}) \end{aligned} \tag{4.2}$$

Thermal Energy Balance:

$$\frac{\partial \rho_f \varepsilon_f C_{p,f} T_f}{\partial t} + \nabla \cdot (\rho_f \varepsilon_f u C_{p,f} T_f) = \nabla \cdot (k_f \varepsilon_f \nabla T_f) + Q_{p,f} \tag{4.3}$$

Species Balance:

$$\frac{\partial}{\partial t}(\varepsilon_f C) + \nabla(\varepsilon_f u C) = \nabla \cdot (D_f \varepsilon_f \nabla C + \Phi) + S_m \tag{4.4}$$

where, Φ is the correction factor for interfacial diffusion (section 4.6.1). The force between the phases, $\vec{F}_{pf}$ is expressed in terms of drag($\vec{f_d}$), lift($\vec{f_l}$), virtual mass force($\vec{f_{vm}}$) and Basset history force($\vec{f_B}$). The force exchange with the importance of each force is discussed in section 4.4.

4.2 Volume of Fluid (VOF)

In the VOF method, multiple continuous phases are represented by a single set of Navier-Stokes equations and an additional transport equation for the phase fraction 4.5 [5].

$$\frac{\partial(\alpha)}{\partial t} + \nabla \cdot (\alpha u_f) = 0 \tag{4.5}$$

where α is the volume fraction of the fluid such that $\sum_{i=1}^{nphases} \alpha_i$ is unity, u_f is the fluid velocity. When a particle phase is considered, void fraction is introduced to the equation. In OpenFOAM®, to maintain the sharpness of the interface region, an artificial compression term is added to the transport equation as shown in equation 4.6 [60].

$$\frac{\partial(\varepsilon_f \alpha)}{\partial t} + \nabla \cdot (\varepsilon_f \alpha u_f) + \nabla \cdot (\varepsilon_f \alpha (1-\alpha) u_c) = 0 \tag{4.6}$$

where u_c is a velocity field suitable to compress the interface. This artificial term is active only in the interface region due to the term $(\alpha(1-\alpha))$.

With different fluid phases present in a cell, the field mixed properties are obtained as a weighted averaged of the volume fraction of the fluids as shown in equations 4.7 - 4.9.

$$\langle\rho\rangle = \sum_{i=1}^{nphases} \alpha_i \rho_i \qquad \langle\nu\rangle = \left[\sum_{i=1}^{nphases} \frac{\alpha_i}{\nu_i}\right]^{-1} \tag{4.7}$$

$$\frac{\langle\rho\rangle\langle C_p\rangle}{\langle k\rangle} = \sum_{i=1}^{nphases} \frac{\alpha_i \rho_i C_{p,i}}{k_i} \qquad \langle D\rangle = \left[\sum_{i=1}^{nphases} \frac{\alpha_i}{D_{C,i}}\right]^{-1} \tag{4.8}$$

$$\langle\rho\rangle\langle C_p\rangle = \sum_{i=1}^{n_{phases}} \alpha_i \rho_i C_{p_i} \qquad \langle C_s\rangle = \sum_{i=1}^{nphases} \alpha_i C_{s,i} \tag{4.9}$$

4.3 Discrete Element Method

The Discrete Element Method was introduced by Cundall and Strack (1979) [23]. It is a Lagrangian method where the particles in the system are tracked explicitly based on the momentum balances for transnational and angular acceleration as shown in equations 4.10 and 4.12 respectively.

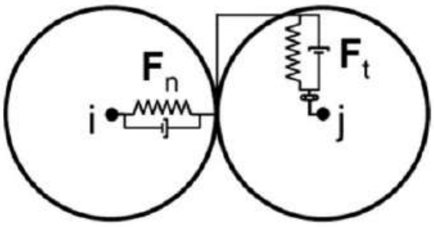

Figure 4.1: Simple spring dashpot model

In a DEM simulation the trajectory of particles are based purely on the collisions with other particles and the walls. The method stretches a collision over several time steps and calculates the resultant force and assigns the trajectory via Newtons laws of motion. The contact force is decomposed into a normal and tangential force. The complex contact-mechanical behavior of colliding particles are approximated by simple spring-dashpot models (Fig.4.1) [26].

$$m_{p,i}\frac{du_{p,i}}{dt} = F_{f\rightarrow p,i} + F_{C,i} + m_{p,i}g \tag{4.10}$$

where, $m_{p,i}$ is the mass of the particle, $F_{f\rightarrow p,i}$ is the force due to fluid-particle interactions (discussed in section 4.4, $F_{C,i}$ is the contact force due to particle-particle or particle-wall interactions given by,

$$F_{C,i} = \sum_{j\neq i}[F_{C,ij,n} + F_{C,ij,t}] \tag{4.11}$$

Normal contact force:

$$F_{C,ij,n} = k_n\delta_n\hat{n}_{i,j} - \eta_n v_{ij,n}$$

Tangential contact force:

$$F_{C,ij,t} = \begin{cases} k_t\delta_t\hat{t_i j} - \eta_t v_{ij,t}, & \text{if } |F_{C,ij,t}| \leq \mu|F_{C,ij,n}| \\ -\mu|F_{C,ij,n}|\hat{t_i j}, & \text{if } |F_{C,ij,t}| > \mu|F_{C,ij,n}| \end{cases}$$

where, I_i is particle moment of inertia, $\Omega p, i$ is the angular velocity of particle and $T_{t,i}$ describes the torque on particle i caused by tangential forces.

$$I_i\frac{d\Omega_{p,i}}{dt} = T_{t,i} \tag{4.12}$$

for,

$$T_{t,i} = \sum_{j\neq i}T_{t,ij} = \sum_{j\neq i}(-R_{p,i}\hat{n}_{ij} \times F_{C,ij,t})$$

where, k is the spring stiffness, δ is the overlap, η is the damping coefficient and μ is the coefficient of friction.

4.4 CFD - DEM Coupling

An approach which combines a discrete method for particles and a continuum model for the fluid is referred to as a Eulerian-Lagrangian (E-L) method. The interactions between the two phases are then coupled by exchange terms.

The process of predicting the dynamics of a multi-phase system through CFD-DEM can be done by two means: Resolved or Unresolved methods. The method of resolved CFD-DEM considers a system with large particles that spread over multiple CFD cells. The interaction between the two phases are resolved over multiple cells providing a resolved flow between particles as shown in figure 4.2. This method is quite computationally expensive and is limited to systems with small number of particles (a couple hundred). The later approach, unresolved method consists of a system where the particles are smaller than the CFD cells. The common practice shows the ratio between the cell dimension and the diameter of the particle lies in the range of 3-7. Here a CFD cell contains multiple particles and the flow between the particles is not resolved. This method can be applied to systems with large number of particles packed densely.

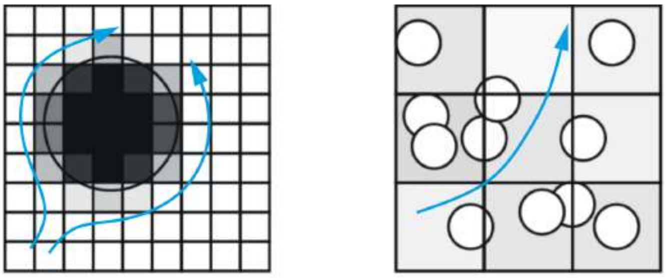

Figure 4.2: left:flow around the particle is resolved; right:unresolved CFD where flow around the particles is modelled.

In this research, two way coupling and unresolved approach is considered to efficiently predict the dyanmics of a blast furnace hearth. The major forces that are coupled between the two phases are: drag force, lift force, virtual mass force and Basset history force. The first two forces are commonly used in most of the simulations while the latter two are usually ignored as they display less significance. Hence they are commonly neglected with few assumptions made during modelling. Further, the resolution of the later two forces commonly referred to as unsteady forces is computationally expensive. But in case of a blast furnace consisting of molten iron with high viscosity and density, the unsteady forces exhibit relative significance in the dynamics of the system.

Drag

An object in a fluid experiences a steady state force acting opposite to the relative motion of fluid. There has been extensive research to quantify the drag force for various systems. The model developed utilises a correlation to represent the drag force in a poly dispersed system as proposed by Beetstra et al. (2007) [61]. The following equation is found to be suitable for mono and poly-dispersed spheres.

$$f_{d,i} = \frac{\pi}{8} d_{p,i}^2 \rho_f C_{d,i} |u_i - v_i| (u_i - v_i) \tag{4.13}$$

$$\begin{aligned} C_{d,i} = \frac{24}{Re_{p,i}} & \left[10 \frac{1-\varepsilon_{f,i}}{\varepsilon_{f,i}^2} + \varepsilon_{f,i}^2 (1 + 1.5\sqrt{1-\varepsilon_{f,i}} \right] \\ & + \frac{0.413}{\varepsilon_{f,i}^2} \left[\frac{\varepsilon_{f,i}^{-1} + 3\varepsilon_{f,i}(1-\varepsilon_{f,i}) + 8.4 Re_{p,i}^{-0.343}}{1 + 10^{3(1-\varepsilon_{f,i})} \cdot Re_{p,i}^{[1+4(1-\varepsilon_{f,i})]/2}} \right] \end{aligned} \tag{4.14}$$

Lift

The force experienced by a particle perpendicular to the fluid flow is known as lift force. The force perpendicular to the flow due to the velocity gradient along the particle is known as Saffman lift. On the other hand, the force perpendicular to the flow due to rotation is called the Magnus lift. The above two types of lift is incorporated into the model as represented by Mei et al. (1992) [62] and Loth et al. (2008) [63].

$$\begin{aligned} f_{l,i} = \frac{\pi}{8} d_{p,i}^2 \rho_f & \left[C_{l,\omega,i} |u_i - v_i|^2 (u_i - v_i) \times \omega_i \right] \\ & + C_{l,\Omega,i} d_{p,i} (u_i - v_i) \times \Omega_i \end{aligned} \tag{4.15}$$

$$C_{l,\omega,i} = \left\{ 1 + tanh \left[\frac{5}{2} (log_{10}(\sqrt{\frac{\omega_i^*}{Re_{p,i}}} + 0.191 \right] \right\} \cdot \\ \left\{ \frac{2}{3} + tanh \left[6(\sqrt{\frac{\omega_i^*}{Re_{p,i}}} - 0.32) \right] \right\} \cdot \frac{3.876}{\pi} \sqrt{\frac{\omega_i^*}{Re_{p,i}}} \tag{4.16}$$

with $\omega_i^* = \frac{|\omega_i| d_{p,i}}{|u_i - v_i|}$

$$C_{l,\Omega,i} = \Omega_i^* \left\{ 1 - \left[0.675 + 0.15 \Big(1 + tanh \big[0.28 (\Omega_i^* - 2) \big] \Big) \right] \cdot tanh \left(0.18 \sqrt{Re_{p,i}} \right) \right\} \tag{4.17}$$

with $\Omega_i^* = \frac{|\Omega_i| d_{p,i}}{|u_i - v_i|}$

Virtual mass force

When a body is accelerated through a fluid, there is a corresponding acceleration of the fluid which is at the expense of work done by the body [64]. This additional work relates to the virtual mass force that are experienced by the other particles in the neighborhood. The virtual mass force is expressed as [64]:

$$f_{vm,i} = C_{vm,i} \rho_f V_{p,i} \left[\frac{Du}{Dt} - \frac{du_s}{dt} \right]_i \tag{4.18}$$

where,

$$C_{vm,i} = C_{vm,0} + \sum_{k=1}^{3} \left\{ \left[a_{k,0} + a_{k,1} ln(\frac{\rho_{p,i}}{\rho_f}) \right] \cdot (1 - \varepsilon_{f,i})^k \right\} \tag{4.19}$$

Basset history force

Basset history force is a force related to the history of acceleration of a particle. The Basset term accounts for the viscous effects and addresses the temporal delay in boundary layer development as the relative velocity changes with time. It is only relevant to unsteady flows involving a history integral.

Parmar et al. (2018) presented an efficient method to incorporate the Basset history force into the models [65]. The same concept has been implemented in the model by Nijssen et al. (2020) [66].

4.5 Heat transfer in Blast furnace hearth

The blast furnace hearth consists of coke particles at approximately 2000°C, molten metal at about 1600°C, while the walls of the blast furnace are maintained about 400°C. These components at different temperatures give rise to large temperature gradients and results in heat transfer. We can identify the paths of heat transfer as:

1. Conduction through the particle bed
2. Heat transfer between the coke particle bed and molten metal
3. Conduction and convection in molten metal
4. Heat transfer between the walls of the hearth and its contents (molten metal and coke particles)

Heat transfer through radiation is a common path for systems at high temperature. Despite the high temperatures of operation, radiation inside the hearth is found to be less significant. This can be shown by the Stark number, expressed as the ratio between the radiation and conduction [67][68]. The value of Stark number was observed to be <1 which indicates heat transfer is majorly driven by conduction. Therefore, radiative contributions were ignored.

$$Stark\ number: \quad Sk = \frac{\varepsilon \sigma_o T^2 L}{k} = 0.3861 \tag{4.20}$$

with emissivity of coke, $\varepsilon = 0.95$ [-]; Stefan-Boltzmann constant,$\sigma_o = 5.67 \cdot 10^{-8} [W/m^2K^4]$; $T = 2273$K the temperature of particle, L, the diameter of particle.

4.5.1 Heat transfer between the particles

The particles in the hearth are at different temperatures and are constantly in contact. The heat transfer occurs through the contact area between the particles. This path of heat transfer is expressed in terms of a correlation provided by Chaudhuri et al. (2006) [33]

$$H_c = 4k_{eff,p} \left[\frac{3F_N r^*}{4E^*} \right]^{\frac{1}{3}} \tag{4.21}$$

$$Q_{i,j} = H_c \left(T_j - T_i \right) \tag{4.22}$$

where, H_c is the inter-particle conductance, $k_{eff,p}$ is the effective thermal conductivity of two particles, T_i and T_j temperatures of the two particles, F_N is the normal force, E^* is the effective Young's modulus for the two particles, and r^* is the geometric mean of the particle radii.
Hertz contact model proposes an equation to calculate the contact area between two particles in contact. Equation 4.23 gives the radius of the circular contact area between two spheres. Equation 4.24 is obtained by combining the equations 4.22 and 4.23.

$$a = \sqrt[3]{\frac{3F_N r^*}{4E^*}} \tag{4.23}$$

$$H_c = 4k_{eff} \sqrt{\frac{A_{cont}}{\pi}} \tag{4.24}$$

where, a is the radius of contact area.
LIGGGHTS® incorporates a geometric analytical equation to calculate the radius of circular contact area as shown in equation 4.25 [69]:

$$a = \frac{1}{2r} \sqrt{(-r + r_i - r_j)(-r - r_i + r_j)(-r + r_i + r_j)(r + r_i + r_j)} \tag{4.25}$$

where, r is the distance between the particle centers, r_i and r_j is the radius of the particles.

4.5.2 Particle - Fluid Heat transfer

The correlation proposed by Gunn (1978) is used to model the heat transfer between the particles and the fluid [37]. The Nusselt number is correlated with void fraction, Reynolds and Prandtl numbers. The heat transfer between the fluid and particles is expressed as [70],

$$Q_{pf} = h_{p,f} A_p \Big[T_f - T_p \Big] \tag{4.26}$$

$$h_{p,f} = \frac{k_f}{d_p}(7 - 10\epsilon + 5\epsilon^2)(1 + 0.7Re^{0.2}Pr^{\frac{1}{3}}) + (1.33 - 2.4\epsilon + 1.2\epsilon^2)Re^{0.7}Pr^{\frac{1}{3}}, \tag{4.27}$$

$$\text{for,} \qquad 1 < Re < 10^3, \qquad 0.6 < Pr < 380, \qquad 0.35 < \varepsilon < 1$$

where, Q_{pf} is the heat transferred between the two phases, h_{pf} is the heat transfer coefficient and d_p is the particle diameter.

4.5.3 Heat transfer through conduction

A packed bed consists of an irregular distribution of particles in the bed. This results in varied void fractions in the cells of the system. Heat transfer through conduction in the fluid as a result is found to be non uniform. Effective thermal conductivity is introduced into the model to evaluate the conduction. The effective thermal conductivity as mentioned in the Zehner-Bauer-Schlunder model (ZBS model) is a function of void fraction and thermal conductivity. Syamlal et al.'s rendition of this model provides for a correlation that neglects radiation and splits the terms into fluid and particle counterparts [71]. Hence, for our model, the fluid part of the equation was utilised as heat transferred through solids already implemented as stated in section 4.5.1.

$$k_{eff,f} = (1 - \sqrt{1 - \varepsilon_f})k_f \tag{4.28}$$

4.5.4 Wall heat transfer

To model the heat transfer from the walls, a method proposed by Yagi and Wakao (1959) was utilised in the model [39].

Yagi et al. (1959) conducted numerous heat transfer experiments with different types of solids and different particle diameter to tube diameter ratios where the packed beds were heated through the walls. During experiments, the effect of thermal conductivity of the solids was found to be negligible. Additionally, the Prandtl number was observed to be constant and therefore its influence was neglected. The resulting wall transfer coefficient (h_w) was compared to the particle Reynolds number. The authors obtained an empirical formula based on the experimental results was obtained. The heat flux from the walls to the system (bed of particles and the fluid) was expressed as a function of particle Reynolds number as shown in equation 4.30.

$$\frac{h_w D_p}{k_f} = 0.18 Re_p^{0.80} \tag{4.29}$$

with a constant Prandtl number (Pr = 0.70) the expression was re-written as

$$J_H = 0.20 Re_p^{-0.20} \qquad \text{where} \qquad J_H = \left(\frac{h_w}{C_p G}\right)\left(\frac{C_p \mu_f}{k_f}\right)^{2/3} \tag{4.30}$$

h_w is the wall heat transfer coefficient, G is the superficial mass velocity of the fluid.

Further, Yagi et al. (1959) also provided a method to estimate the amount of heat transferred from the walls theoretically. Here, the following assumptions were made:

1. The effective fluid velocity is 9 times the superficial velocity of the fluid.
2. The boundary layer of fluid at the wall is described by the discontinuous boundary-layer model where, the average length of each boundary layer is equal to the diameter of solid particle.
3. The rate of heat transfer in the boundary layer is similar to that of a flow over a flat plate.

The mean heat transfer coefficient was given by:

$$\frac{h_w x}{k_f} = 0.036 Pr^{\frac{1}{3}} \left(\frac{x v \rho_f}{\mu_f} \right)^{0.8} \tag{4.31}$$

substituting the velocity v with $9u_0$ and D_p for x,

$$J_H = \frac{h_w}{C_p G} Pr^{\frac{2}{3}} = 0.2087 \left(\frac{D_p u_0 \rho_f}{\mu_f} \right)^{-0.20} \tag{4.32}$$

Although the equation 4.32 is similar to equation 4.30, the theoretical equation obtained describes only the heat that is transferred from the walls to the fluid. This showed that the influence of the solid thermal conductivity during the experiments were indeed negligible.

In the model, the heat transfer between the walls and the fluid is evaluated with the above correlation. The heat transfer between the particles and the wall was intended to be evaluated using LIGGGHTS®. Here, the wall is considered as an infinitely large particle and the conduction of heat during contact with the particle is evaluated as described in section 4.5.1.

4.6 Mass transfer in Blast Furnace Hearth

In a blast furnace hearth, the coke particles slowly dissolve in the liquid metal. Alongside this process, the carbon present in the refractory bricks also dissolves into the molten metal. The latter of the two transfer processes is observed to be a slow process that occurs over months if not years. Hence, in this study the carbon transfer from the walls to the liquid is neglected for the time scale of simulation.

4.6.1 Diffusion and Correction for diffusion

The diffusion of a specie in a single cell is hindered with the presence of particles. To account for this, an effective diffusivity is calculated similar to effective thermal conductivity. As explained in section 4.5.3, the effective diffusivity is obtained as a function of diffusivity and void fraction.

$$D_{eff} = \left[\frac{1-\sqrt{1-\varepsilon_f}}{\varepsilon_f}\right]\langle D\rangle \tag{4.33}$$

The local concentration of a chemical species k in a phase i is governed by equation 4.34 [72].

$$\frac{\partial}{\partial t}(\varepsilon_i C_{i,k}) + \nabla\cdot(\varepsilon_i u_k C_{i,k}) = -\nabla\cdot(J_{i,k}) + S_m \tag{4.34}$$

where, $J_{i,k} = -D_{i,k}\cdot\nabla C_{i,k}$ is the flux given by Fick's law. At the interface, the concentration of a species can be discontinuous due to difference in solubility between the two phases [73]. The model developed uses VOF where, one species balance equation is solved for the n phases. In a cell located in the interface, a correction for this difference in solubility must be applied. Therefore, a correction flux is introduced based on Henry's constant (He) as shown in equation 4.35 to determine the concentration profile [72].

$$\Phi = -\langle D\rangle\frac{C(1-He)}{\alpha_{liq}+He(1-\alpha_{liq})}\nabla\alpha \tag{4.35}$$

$$C_{air} = He\cdot C_{liq} \tag{4.36}$$

4.6.2 Mass Transfer between Solid and Fluid phases

The transfer of carbon between the particles and the molten iron can be expressed as a function of concentration gradient and mass transfer coefficients.

$$S_m = \sum_{i=1}^{N_p}\left[K_m\cdot\frac{A_{int}}{V_{cell}}(\langle C_s\rangle - C)\right] \tag{4.37}$$

where, N_p is the number of particles, K_m is the rate of mass transfer, A_{int}, V_{cell} are the interfacial surface area and volume of the cell and C_s is the saturation concentration of carbon in molten iron.

Similar to the heat transfer, the mass transfer constant is calculated from the correlation proposed by Gunn (1978) [37]. The mass transfer coefficient is calculated with Sherwood number (Sh) which is expressed as a function of Reynolds number and Schmidt number as shown in equation 4.38. For a blast furnace the average $Sc \sim 90$ while the Re is usually in the magnitude of $1\cdot 10^2$.

$$K_m = \frac{D}{d_p}(7-10\epsilon+5\epsilon^2)(1+0.7Re^{0.2}Sc^{\frac{1}{3}}) + (1.33-2.4\epsilon+1.2\epsilon^2)Re^{0.7}Sc^{\frac{1}{3}}, \tag{4.38}$$

$$\text{for,}\quad 1 < Re < 10^3,\qquad 0.6 < Sc < 380,\qquad 0.35 < \varepsilon < 1$$

The mass transfer coefficient for the carbon dissolution in molten metal was experimentally determined by Gudenau et al. (1990) and Jones et al. (1998) [56][74]. The coefficient of transfer is expressed as

$$K = k_0(u)^{0.7} \cdot \exp\left(-k_0(u)^{0.7} \cdot \frac{A_{int}}{V_cell} \cdot t\right) \tag{4.39}$$

where, k_0 is a constant ($k_0 = 0.00211$), A_{int} is the surface area of particle in contact with the fluid, t is the time.

The above equation also accounts for the ash layer formation observed on the coke particles when immersed in molten iron. For more detailed analysis of the mass transfer, equation 4.39 can be utilised in the model to obtain the mass transfer coefficient.

4.6.3 Shrinking of Particles

The coke particles undergo dissolution in the molten iron phase and hence the size of the particles shrinks with time. The process of shrinking is expressed in the model as a function of mass transfer and time. It is assumed that during this process, the density of the particle remains constant. The amount of mass transferred is calculated by equation 4.41 and the new radius of the particle is calculated as,

$$r_p^{n+1} = r_p^n - \sqrt[3]{\frac{3\Delta m}{4\pi\rho_p}} \tag{4.40}$$

for,

$$\Delta m = K_m \cdot A_{int}\,[\langle C_s\rangle - C] \cdot \Delta t \tag{4.41}$$

where, r_p^{n+1} is the radius of particle for $n+1$ time step.

Chapter 5

Experimental Results and Discussions

5.1 Fluid flow

Before the experimental runs were recorded for particle movement, certain checks were performed to evaluate the components of the setup. First, the flow of water in and out of the system was evaluated. The hearth was filled with particles and inflow rate of water was set to 0.75 L·min^{-1}. The hearth was allowed to fill up with water and the procedure for draining the system was enabled. This allowed for the water to fill into the system and exit the system as described in section 3.2.3. This process was carried out for 900s and the in and out flow rates of water was recorded for all the inflow rates as shown in figure 5.1.

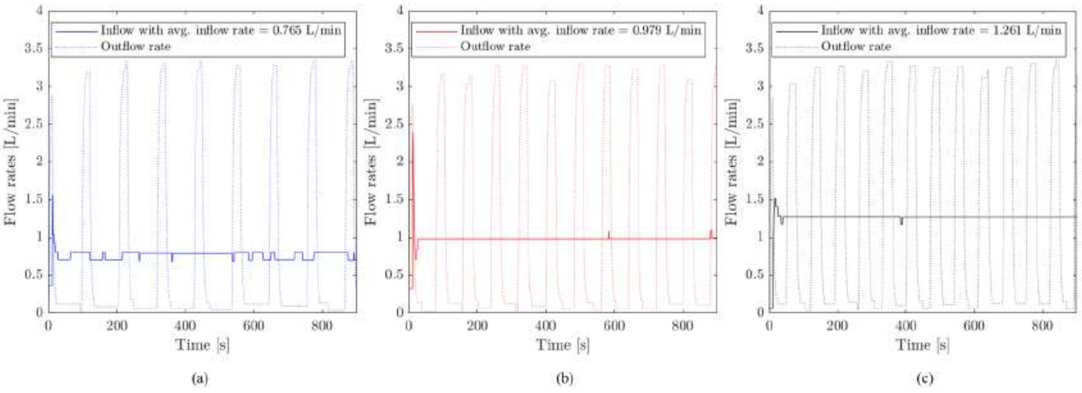

(a) (b) (c)

Figure 5.1: Analysing the inflow and outflow rates of the experimental runs; (a) Inflow rate = 0.75 L·min^{-1}; (b) Inflow rate = 1.00 L·min^{-1}; (c) Inflow rate = 1.25 L·min^{-1};

The inflow rates of the fluid was analysed to evaluate the performance of the flow controlled pump in maintaining the set flow rate. The outflow rates of the fluid was analysed to initially check the smooth operation of the taphole valves during drainage. This drainage rate was used to obtain the key parameters in describing the outflow rates in the simulation.

5.2 Force controller calibration

After setting the flow of water into and out of the system, process of moving the burden plate with the bed was evaluated. The PID controller moves the burden plate according to the difference between the desired set point and the measured process value. The PID controller is described by equation 5.1 [75].

$$G_{PID}(s) = K_p\left(1 + \frac{1}{sT_n} + \frac{sT_v}{1 + sT_d}\right) \tag{5.1}$$

where, K_p (Controller amplification), T_n (Integral action time), T_v (Derivative action time) and T_d (Damping time).

Table 5.1: Values for parameters selected for optimising the PID control and burden plate movement with the bed.

	Run 1	**Run 2**	**Run 3**
K_p [-]	0.6	0.55	0.6
T_n [s]	0.3	0.55	0.5
K_v [s]	0	0	0
K_d [s]	0	0	0
Average force [N]	2.9103	2.0104	2.0079

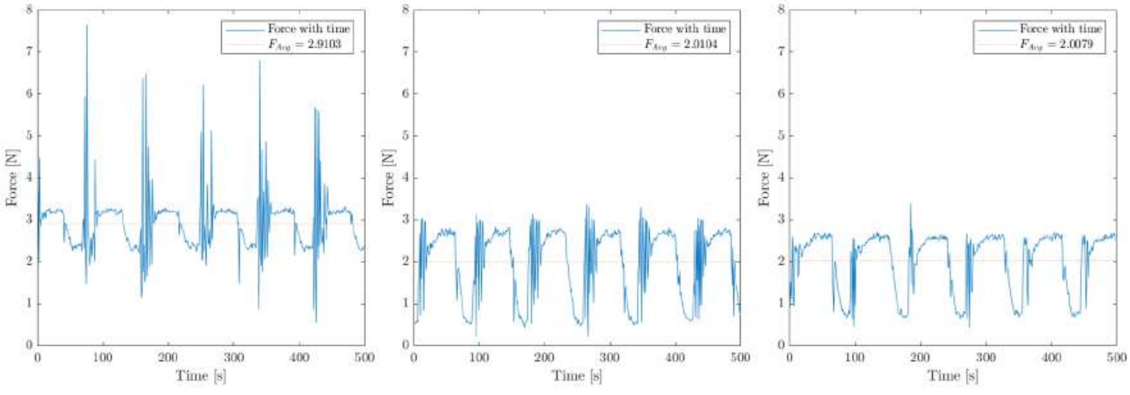

Run: 1 Run: 2 Run: 3

Figure 5.2: Optimisation of PID control for burden plate movement with different values for the parameters of equation 5.1; The results of selected parameters are shown on the right.

First a set of values were assigned for the parameters of equation 5.1 as shown in table 5.1 and the controller was switched on. The setup was undisturbed for few minutes and then the periodic movement of bed was induced by the flow. The burden plate was allowed to move with the bed using the PID controller. The force on the bed was recorded and the PID control of plate movement with the bed was evaluated. The process was repeated with optimising the values of parameters till an average force of 2.0079N was achieved (figure 5.2).The used parameter sets are shown in table 5.1.

5.3 Moving bed and Particle position

As the experimental run was started, the MPT system starts to collect data on the particle position. The particles in the bed is subjected to two main external forces, (1) the the upward buoyant force applied by the water and (2) the downward force applied by the burden plate.

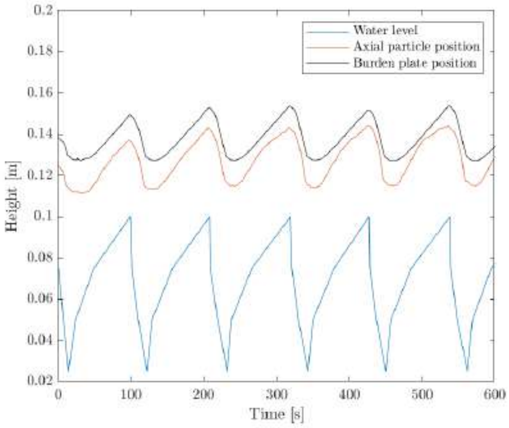

Figure 5.3: (a) Comparing the level of water in system to the axial position of particle and burden plate with time to analyse the movement of bed and the plate.

A run of 600s was conducted with the water level in the system rising and dropping periodically over time. The burden plate was activated to apply force on the particles using the PID controller. With the aforementioned forces acting on the particles, the position of particles must be synchronous with the water level. This is observed in figure 5.3 (a) where the particle follows a similar periodic axial movement comparable to the level of water with time. Furthermore, with the axial change in particle position, the burden plate also has to move with the bed in order to apply constant force. As expected, the plate is observed to move with the bed of particles, applying the set constant force. This can be seen in figure 5.3 (b). All of the axial positions pertaining to the water level, particle and plate positions shown in figure 5.3 are measured from the base of the hearth.

5.4 Fluid flow and particle migration

With the initial checks performed, experiments were performed as described in section 3.4. With the MPT system, burden plate controller, recycle turned on, the data was recorded for 900s. The procedure was repeated for the different inflow rates and the results of the axial and radial particle position with time is compared in figure 5.4 and figure 5.5 respectively.

With a higher flow rate it is observed that the number of tapping cycles increases for the same duration of 900s. It is also noticed that the average particle position during each cycle is changing over time. The particle migration (axial and radial) is noted to increase with the number of cycles. As shown in the figures 5.4 and 5.5, the particle position is largely influenced by the level of water in the system and follows a wave like pattern. To assess the true re-arrangement of particle, the following calculation was done. The initial particle position was recorded with the level of water that was present in the system during measurement. The particle position was recorded again when the level of water reached the initial level recorded. This was continued for the total time of 900s. A net migration value was calculated for the particle with the initial and final reading of particle position corresponding to same water level as,

$$\text{Net Axial Migration} = z_p(t = 0, z_f = h_0) - z_p(t \approx 900, z_f = h_0)$$
$$\text{Net Radial Migration} = r_p(t = 0, z_f = h_0) - r_p(t \approx 900, z_f = h_0)$$

where, z_p and r_p are the axial and radial positions of the particle, while z_f is the level of water in the system.

A net migration distance of a particle was calculated for each of the runs. The results are compared in table 5.2.

Table 5.2: Net migration of particle in the bed as a result of different inflow rates of water.

	Inflow rate of water		
	0.75 [L/min]	**1.00 [L/min]**	**1.25 [L/min]**
Net Axial Migration / d_p [-]	5.24	6.72	9.16
Net Radial Migration / d_p [-]	1.84	2.52	3.12

The bed is initially resting on the bottom of the hearth with the burden plate applying a force from the top. During this time, the bed is compactly packed between the bottom of the hearth and the plate above. As the water flows into the system, the bed starts to float and the burden plate moves up with the bed. In a floating bed, the particles are pushed from the top by the plate while the particles at the bottom are freely floating in water. This relaxes the packing of the bed and the bed expands slightly when compared to before. This allows the particles to re-arrange themselves in the bed. The magnitude of re-arrangement may be small during a single cycle of tapping, but over time, the migration of particles due to re-arrangement sums up. This explains the higher particle migration observed during the runs with higher inflow rates as shown in table 5.2.

With higher frequencies of tapping, the rearrangement in bed is increased. As a result, the void fraction of bed could also increase. This would allow for a better seepage of fluid through the bed resulting in lower circumferential flows. During the experiments, the void fraction in the bed could not be measured. Hence using the simulations, the void fraction of the bed was checked. This will be further discussed in section 6.1.4. Further, debris in the bulk of the deadman also migrate with the particles through the bed. This allows the debris to combine with the slag layer. Chapman et al. (2011) also provided similar analysis on coke particle behaviours in the hearth of a blast furnace [76].

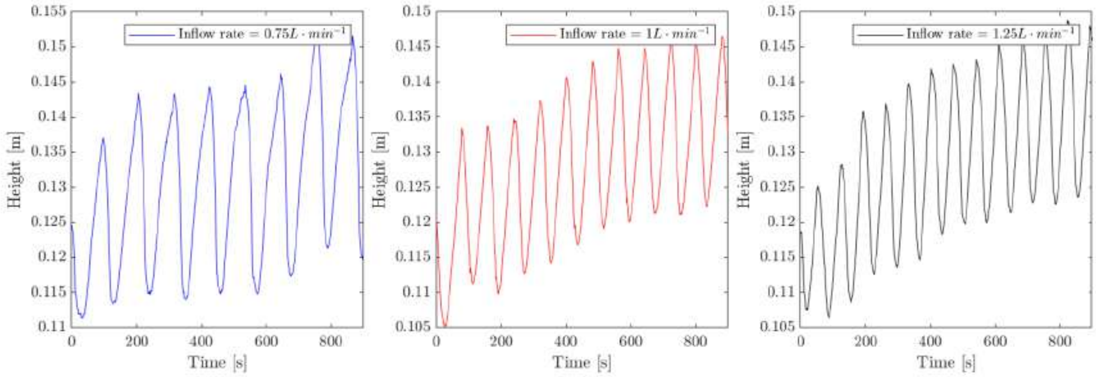

(a) (b) (c)

Figure 5.4: Comparing axial particle positions with different inflow rates of water;
(a) Inflow rate = 0.75 L·min^{-1}; (b) Inflow rate = 1.00 L·min^{-1}; (c) Inflow rate = 1.25 L·min^{-1};

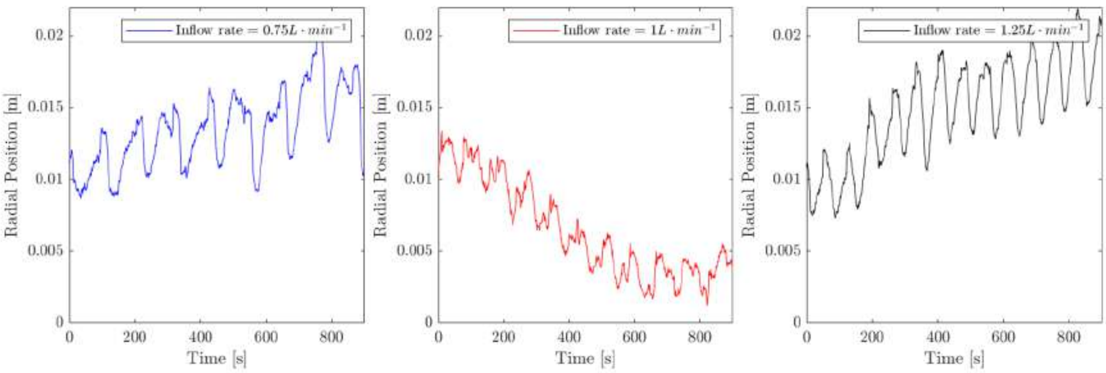

(a) (b) (c)

Figure 5.5: Comparing radial particle positions with different inflow rates of water;
(a) Inflow rate = 0.75 L·min^{-1}; (b) Inflow rate = 1.00 L·min^{-1}; (c) Inflow rate = 1.25 L·min^{-1};

Chapter 6

Numerical Results and Discussions

6.1 Blast furnace hearth simulations

The data recorded from the experiments is incorporated into the existing model to further analyse the dynamics of the bed. The geometry constructed by Hoeks (2019) was used in this work. A cylindrical geometry was constructed with the similar dimensions of the experimental small scale hearth as shown in figure 6.1.

The tapholes were defined in the geometry close to the positions found in the experimental set up. Due to large nature of the cells found in unresolved CFD-DEM simulations, the tapholes were limited to a single cell at the boundary. For the process of dynamic tapping, a sequential simulation was defined where the boundary conditions of the tapholes were altered for their operation. A burden plate was introduced into the system and was controlled using the *servo* mesh module available in LIGGGHTS® that mimics a PID controller. The raceways in the simulation was implemented as a small patch of volume in the system based on the raceways used in experiments. As a particle approaches this patch in the system, the particle is deleted from the simulation to mimic the function of raceways. Particle recycle was neglected as the number of particles recycled is negligible compared to the total number of particles.

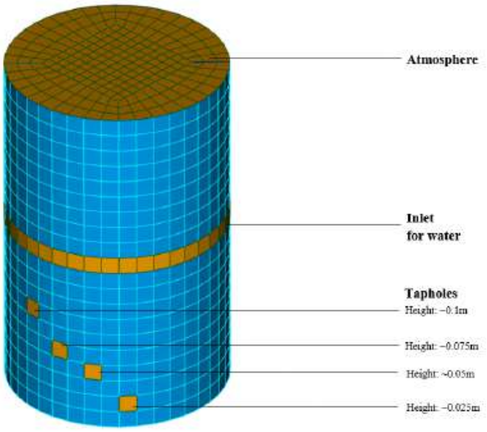

Figure 6.1: Mesh and geometry of the hearth used for the simulations with the geometry similar to the experimental setup with inlets and tapholes.

Table 6.1: Properties and parameters of fluid and solid phases for evaluating the influence of fluid inflow rates on bed dynamics.

Parameters	**Values**	**Units**
Hearth Height	0.3	[m]
Hearth Diameter	0.190	[m]
Average Particle Diameter	$5 \cdot 10^{-3}$	[m]
Number of Particles	34000	[-]
Inflow rate of water	0.75/1.0/1.25	[L/min]
Force by burden plate	2	[N]
Proportional PID term (K_p)	$5 \cdot 10^{-3}$	[-]
Taphole Height	0.025	[m]
Upper switch point for drainage	0.1	[m]
Lower switch point for drainage	0.025	[m]
Friction loss factor	15	[-]
Restitution Coefficient	0.3	[-]
Static Friction Coefficient	0.5	[-]
Rolling Friction Coefficient	0.15	[-]
Average Grid Size	$1.5 \cdot 10^{-2}$	[m]
CFD Timestep	$1 \cdot 10^{-3}$	[s]
DEM Timestep	$1 \cdot 10^{-5}$	[s]

The simulations consisted of $34{\cdot}10^3$ particles with a similar size distributions found in the experimental set up. The particles are of an average radius of 2.5mm and a density of 405 kg·m^{-3}. The simulations consisted of an additional thousand particles when compared to the experimental runs as to account for a large number of particles being deleted in the first few time steps (order of $1{\cdot}10^{-5}s$). The particles were added to the system with initial water level at 0.075m. Further, the PID control of the burden plate was set up using similar K_p values used in the experiments.

The outflow rates described in the simulation was derived from the Bernoulli's principle for conserving energy in in-compressible flows [77]. The Bernoulli's law for flow with internal friction is represented in equation 6.1.

$$\Delta\left(\frac{1}{2}\frac{\langle v^3\rangle}{\langle v\rangle}\right) + g\Delta h + \int_1^2 \frac{1}{\rho}dp = \hat{W_m} - \hat{E_v} \tag{6.1}$$

where, $\hat{E_v}$ is the amount of mechanical energy lost per mass unit fluid and $\hat{W_m}$ is the net amount of mechanical energy supplied per mass units between points 1 and 2. Assuming the velocity to be uniform and no work done on the system, E_v from equation 6.1 can be represented as,

$$\hat{E_v} = \sum_{i=1}^{i=N}\left(\frac{1}{2}v^2\frac{L}{R_h}f\right)_i + \sum_{i=1}^{i=M}\left(\frac{1}{2}v^2 e_v\right)_i \tag{6.2}$$

where, f is the Dracy friction factor, e_v is the friction loss factor, N is the number of straight conduits, M is the number of other equipment such as valves, fittings etc.

The Reynolds number is calculated based on the theoretical maximum velocity in the system. With the flow regime dictated by the Reynolds's number, the value of e_v is calculated from equation 6.3 (for sudden contraction) and f is obtained from the Moody chart.

$$e_v = 0.45(1-\beta) \tag{6.3}$$

where β is the ratio of smaller to larger contraction area.

The periodic opening of the tapholes in the simulation was based on the experimental operations. During experiments, the time corresponding to the open and closing of tapholes were recorded. The recorded time was used to operate the tapholes in the simulations. The parameters used to set the simulation has been described in table 6.1. The simulations with different inflow rates were run for 900s.

6.1.1 Model validation

Dynamics tapping cycles

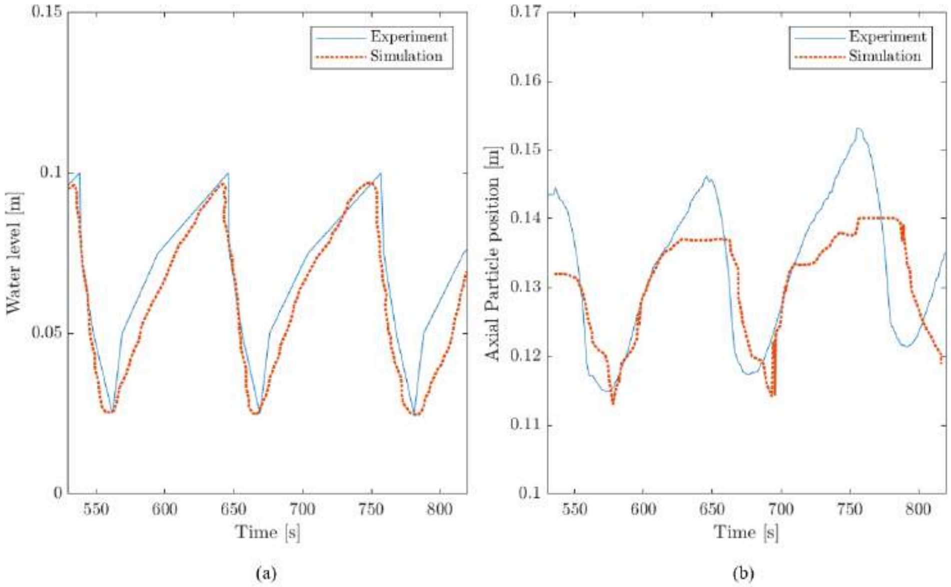

Figure 6.2: (a) Comparing the results of the simulation with the level of water present in the system during experiments; (b) Comparing the axial particle position as recorded by MPT and the results of the simulation.

The model is developed to evaluate a moving packed bed. The change in water level with time as predicted by the model is compared to the experimental data. The water level in the simulation was determined based on the volume fraction of water. At a given time step, the cells at the center of the system were checked for the volume fraction of water. The cells with a volume fraction greater than 0.5 were considered. The axial position of these cells were compared and the cell with the highest axial position was selected. The water level at that time step was determined as the axial position of the cell selected.

$$Water\ level = max\Big(z|_{\alpha_w > 0.5}\Big)$$

where, z is the axial position of cell, α_w is the volume fraction of water in the cell.

As seen in the figure 6.2 (a), the predicted water level in the system is close to the water level observed during experiments. This provides information on the in and the outflow of the system. The rise in water level predicted by the model is closely comparable to the water levels observed during experiments. The rate of decreasing in water level in the simulation is closely comparable to the experimental observations as seen in figure 6.2 (a). This implies that the resistance factors defined in equation 6.2 result in outflow rates similar to those found in experiments.

Moving packed bed

The movement in the bed during experiments can be represented by the axial movement of magnetic tracer particle with time. Similarly, in the simulation, a particle present in the top layer of the bed is considered. The position of the selected particle with time is recorded. The axial positions of the particle with time in the simulation is compared to the MPT data as shown in figure 6.2 (b). The rise and fall in the particle position in the simulation is comparable to the MPT data. The results from the simulation differ slightly from the MPT data as the particle reaches its peak position. The difference observed is a result of the burden plate function in the simulation. It is observed that the burden plate in the simulation halts its movement during these periods and as a result the bed is forced down into the liquid hindering the rise of bed. This can be corrected with further detailed tuning of the `servo mesh module` of LIGGGHTS® implemented to the burden plate to act as a PID controlled system.

Particle migration in the bed

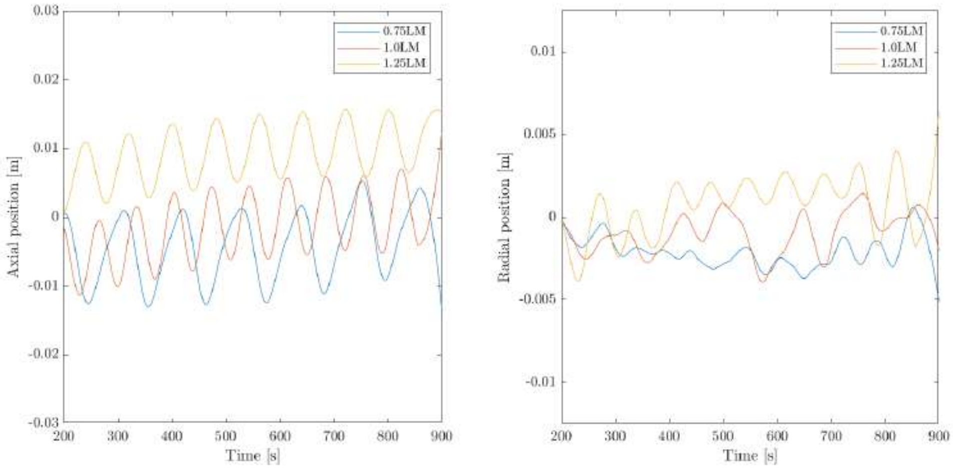

Figure 6.3: Comparing the influence of inflow rate on particle migration inside the bed; (Left) Axial migration of the particle in the bed; (Right) Radial migration of the particle in the bed.

To observe the particle migration in the bed, a single particle was selected in each of the varying inflow rate simulations. As the simulation attained stability, the particle positions were recorded. For a simulation, the particle position over time was normalized by deducting all positions over time by the initial position. The particles now start from zero and migrate over time. The particle's axial and radial positions are compared in figure 6.3(a) and (b) respectively.

The migration of particle is similar to the observations made with the experimental data. Particle migration increases with the increasing inflow rates. As explained in section 5.4, the increase in the number of tapping cycles increase the the frequency of the bed re-arrangement.

6.1.2 Flow profiles and Circumferential flow

After the validation of the model, the model results can be further analysed to observe the flow profiles formed in the system. To observe the water drainage in the simulation, a certain time,t is chosen where the taphole is open. The system is again characterised by the volume fraction of water and the cells that contain $\alpha_w > 0.5$ are considered. The velocity of water at the different points in this section was recorded. For t = 586s, the water level in the system was observed to be about 0.06m from the base of the column. A plane in the xz direction passing through the taphole was selected. Velocity profile was mapped for the plane and velocity vectors were plotted as shown in figure 6.4 (b). The plot shows a higher velocity close to the taphole. The velocity of fluid on the far side of the taphole is comparatively insignificant. This is a common phenomena observed in the large scale blast furnace as well [78]. The higher velocity of fluid close to the taphole exerts greater stress on the walls near the taphole over time.

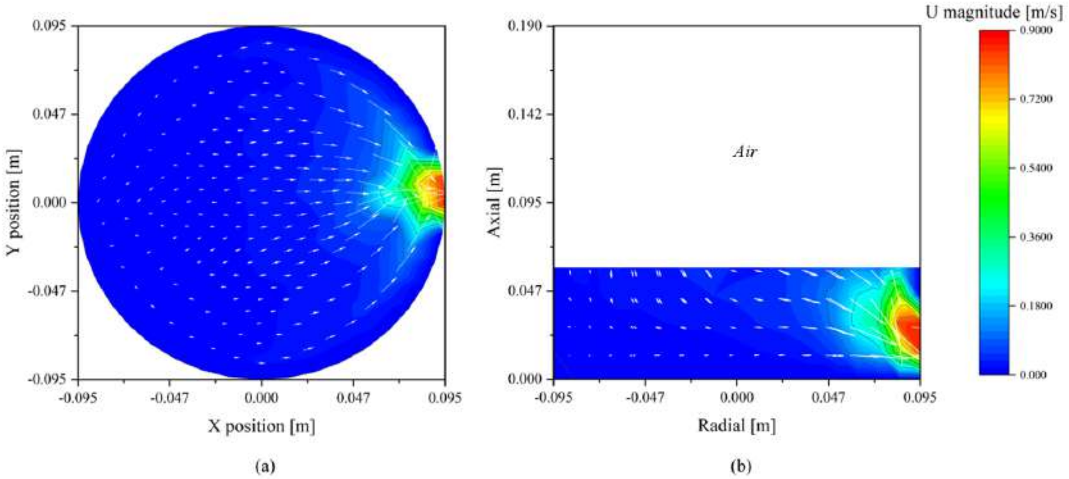

Figure 6.4: (a) Velocity profile of water in a horizontal plane at the height of the taphole. (b) Velocity profile of water in a xz plane when the water level is at 6cm height from the bottom.

Further, an xy plane was considered at the height of the taphole as shown in figure 6.4 (a). The velocity profile of the fluid was mapped on this plane for the same time, t = 586s. Again, the velocity close to the tapholes are significantly larger than the velocity observed in other sections of the plane. In addition, the velocity vectors show a circumferential flow in the system. The fluid is observed to follow a path around the bed of particles before being drained through the tapholes as illustrated in figure 6.4 (a). In a large scale blast furnace, the flow of fluid past the deadman applies greater stress on the walls. Over time, the walls undergo erosion resulting in a shape commonly termed *elephant's foot*, previously in figure 1.3.

6.1.3 Floating bed and fluid flow

As the fluid starts to flow into the system with the taphole closed, the water level rises and the bed starts to float. With further increase in water level, the bed of particles floats completely, leaving a particle-free space at the bottom of the column. As a result of high porosity, the magnitude of velocity in this space is higher when compared to the rest of the column. During tapping the velocity of the fluid present in this section is shown in figure 6.5 (b) while figure 6.5 (a) illustrates the void fraction. For a significant difference to be observed in the velocity map, a yz plane is considered where the taphole is normal to the plane.

Further, in figure 6.5 (a), the bottom corners have the highest porosity. This space in a blast furnace is termed as gutter coke free space. It has been observed that this space (both during a floating bed and a sitting bed), possess relatively higher porosity [79]. With a coke free space, the velocity is observed to be higher and as a result the stress on the walls are increased as well. Therefore, it is a common practice in a blast furnace to include more refractory material in this area as seen in figure 1.3.

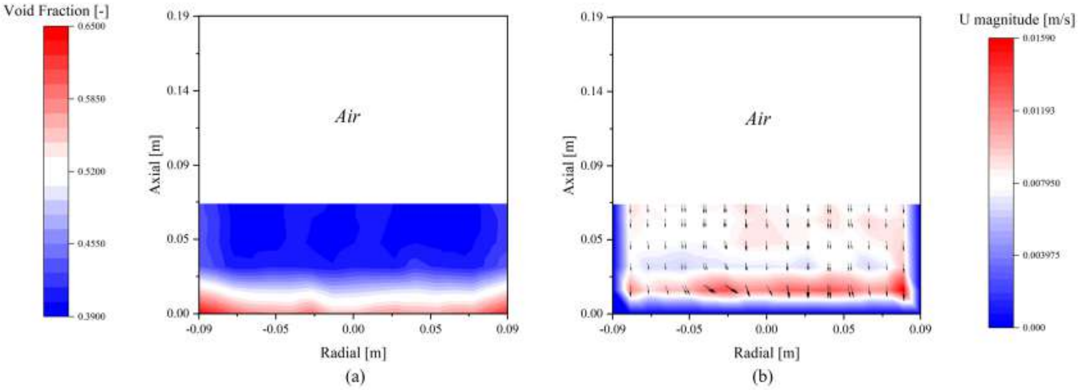

Figure 6.5: (a) Void fraction in the system to illustrate the particle free space at the bottom (b) Velocity profile of water in a xz plane where the velocity of water is maximum in the particle free space.

At time t = 426s, the system had a water level of 0.08m with the particles close to the bottom with no almost particle free space. While at time t = 784s, the water level was observed to be similar but the particle free space was found to be at the height of the taphole. The velocities of the fluid was recorded and compared in figure 6.6. During tapping, the bed of particles close to the taphole offers resistance to fluid outflow. As the particle-free space extends to the height of the taphole, the outflow rates of the fluid is not restricted any longer. As a result, the fluid velocities are greater and the walls close to the taphole experience higher stress. Therefore, blast furnace must be designed with optimum taphole locations to accommodate a floating bed and lower stress on walls during tapping.

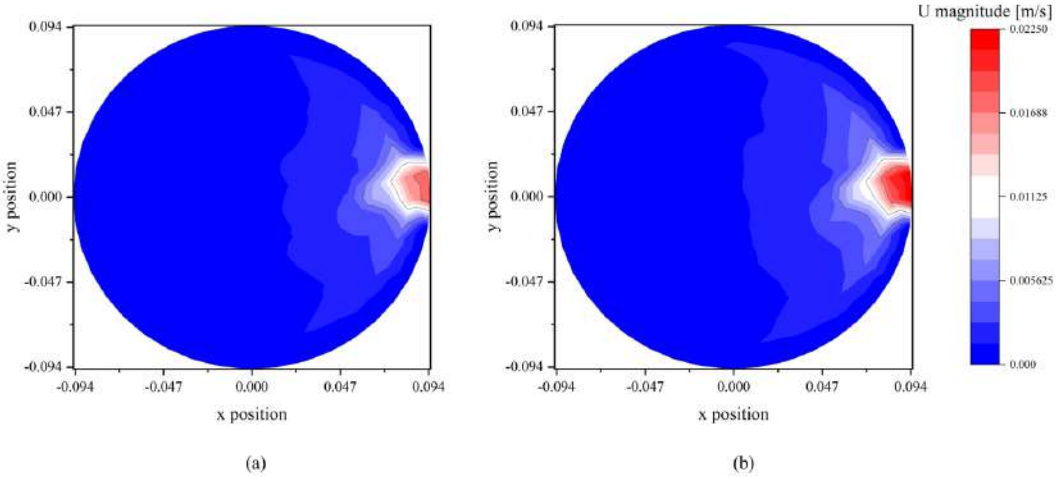

Figure 6.6: (a) Velocity profile of fluid during tapping with the coke particles providing resistance to the flow (b) Velocity profile of water in a xz plane where the velocity of water is unrestricted by the bed of particles.

6.1.4 Influence of inlet flow rates

From the experiments, it was observed that the increase in inflow rates resulted in higher number of tapping cycles. Analysis of the experimental results was limited to the particle positions with time and migration of the particle inside the bed. With the validated model, simulations were run using similar parameters used in the experiments. With the simulation results, the fluid flow and the particle behavior is analysed.

Fluid flow through the bed

A time averaged velocity profile was developed to assess the influence of inflow rates. Between the three inflow rates, comparing the fluid flow at time t, involved various parameter differences. Hence, to focus only on the influence of inflow rates, a time averaged study was performed.

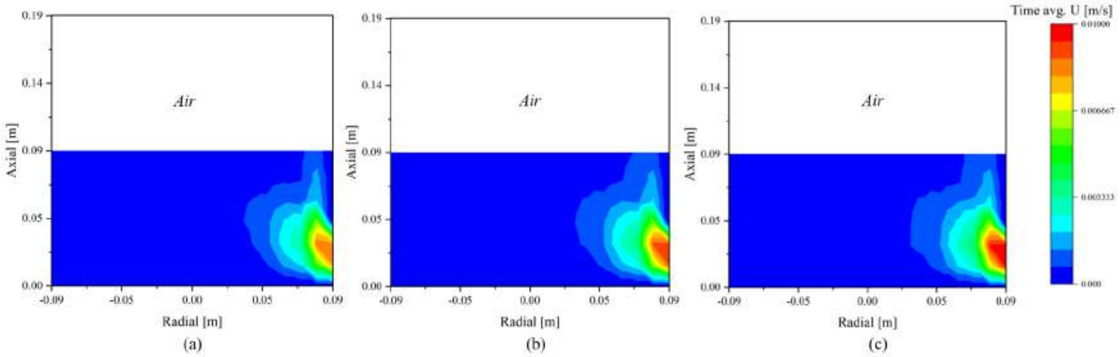

Figure 6.7: Comparing the time averaged velocity profiles observed with different inflow rates; (a) Inflow rate = 0.75 L·min^{-1}; (b) Inflow rate = 1.00 L·min^{-1}; (c) Inflow rate = 1.25 L·min^{-1};

First, at time t=0, the points in the system was checked for the volume fraction of water. Only the points that contained $\alpha_w > 0.5$ was considered. The variables at those points were recorded and corrected for the volume fraction of water. Since the system has varying water levels with time, only the points with $\alpha_w > 0.5$ were recorded at each time step. Finally, the variables were averaged for the period of 900s. This allowed for considering just the parameters of water at each of the points in the system.

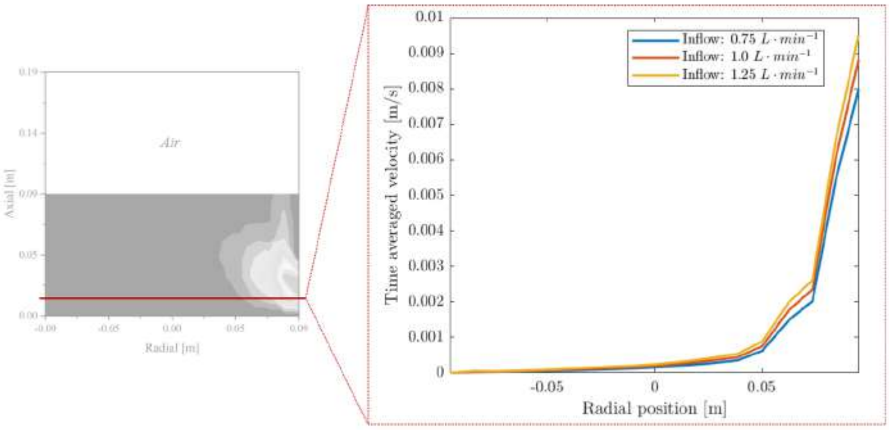

Figure 6.8: Time averaged velocity of fluid over a straight line on xz plane located at the taphole height.

The time averaged velocity profile was developed for each of the inflow rate simulations. The results are compared in figure 6.7. With a higher inflow rate, the frequency of tapping increases.

As a result, the section close to the tapholes experience higher velocities more often. With higher frequencies of tapping, the stress on the walls (close to the tapholes) in a given time period increases. A line on the xz plane at a height of 0.015m from the bottom is selected. The averaged velocity along this line is plotted in figure 6.8 to show the extent in influence of inflow rates.

The rate of heat and mass transfer is a function of fluid velocity. Therefore, with an increase in average velocity, more heat is transferred from the coke particles (at higher temperatures) to the fluid. With higher velocity and temperatures of the fluid, the walls close to the tapholes experience higher magnitudes of thermo-mechanical stress. This increases rates of wear in walls of the furnace during high production rates. Additionally, the amount of energy needed in cooling the walls of the blast furnace is also increased. Hence, the inflow rate of fluid into the hearth of a blast furnace must be optimised to balance between higher production rates and lower wear in walls of the furnace.

In section 5.4, it was estimated that with particle migration and rearrangement, the void fraction in the bed would increase as a function of tapping frequency. To check the prediction, the results of the simulation was analysed. A time averaged void fraction of the bed was calculated. The void fractions were plotted for the three simulations with different flow rates as shown in 6.9. As seen in the figure, for the inflow rate of 0.75 L·min^{-1}, the void fraction in the bulk of the bed is lower compared to the results when inflow rate is 1.25 L·min^{-1}. With this we can suggest that the increased frequency of tapping could lead to greater rearrangement and a more porous deadman.

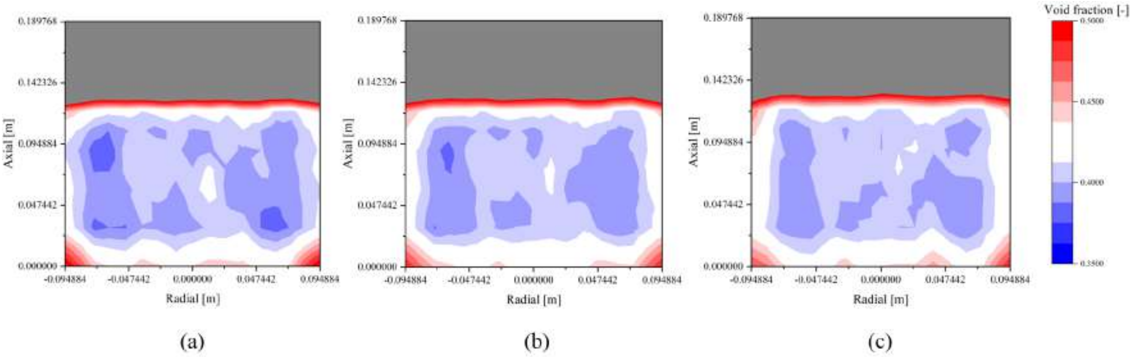

(a) (b) (c)

Figure 6.9: Time averaged void fraction of the bed for different flow rates; (a) Inflow rate = 0.75 L·min^{-1}; (b) Inflow rate = 1.00 L·min^{-1}; (c) Inflow rate = 1.25 L·min^{-1};

6.2 Heat Transfer

6.2.1 Adiabatic heat transfer model

Heat transfer model verification

The heat transfer model developed is verified by comparison with analytical solutions. An adiabatic system is chosen to verify the heat transfer between the solids and the fluid flowing past it with no heat transfer through the walls of the system. A fixed packed bed is opted where the bed and the fluid initially are at a lower temperature. The system is heated by a flow of hot fluid, which heat the particles of the bed. For the heat transfer test air is chosen as the fluid, while spherical alumina particles are chosen as the packing. A portion of the particles are introduced into the system initially and further particle addition is achieved through agitation and finally, an irregular packing with bed porosity of 0.33 is obtained. Other parameters used for the verification is shown in table 6.2.

Table 6.2: Properties and parameters of fluids and solids for verification of heat transfer model.

Parameters	**Values**	**Units**
Bed Height	0.32	[m]
Bed Diameter	0.18	[m]
Particle Diameter	$4.35 \cdot 10^{-3}$	[m]
Void Fraction	0.33	[-]
Cell Size/Particle Dimensions	[2.834 - 3.4256]	[-]
Fluid Viscosity	$19.3 \cdot 10^{-6}$	[Pa· s]
Fluid Density	1.204	[kg/m^3]
Fluid Conductivity	$32.99 \cdot 10^{-3}$	[W/m·K]
Fluid Heat Capacity	$1.006 \cdot 10^{3}$	[J/kg·K]
Particle Density	1570	[kg/m^{-3}]
Particle Conductivity	1	[W/m·K]
Particle Heat Capacity	840	[J/kg·K]
CFD Timestep	$1 \cdot 10^{-3}$	[s]
DEM Timestep	$1 \cdot 10^{-5}$	[s]

The model verification is done by using a one dimensional convection equation with heat transfer between the particle and the fluid phase. The conduction through the fluid is neglected as the Péclet number is found to be $P\acute{e} = 4286$. The following equations were considered for obtaining the analytical solution:

Fluid phase

$$\varepsilon_f \rho_f C_{p,f} \frac{\partial T_z}{\partial t} = -\varepsilon_f \rho_f u_z C_{p,f} \frac{\partial T_z}{\partial z} - K_h a_p (T_z - T_{z,p}) \tag{6.4}$$

Solid phase

$$(1 - \varepsilon_f) \rho_p C_{p,p} \frac{\partial T_{z,p}}{\partial t} = K_h a_p (T_z - T_{z,p}) \tag{6.5}$$

where, K_h is heat transfer coefficient, a_p is the specific interfacial area of the particle. The above two equations were discretised in one dimension to obtain the solutions in MATLAB®.

Figure 6.10 illustrates the heating of the bed and the temperature profile evolution with time. The simulation results are compared to the results of the analytical solution. The solid phase temperature profile generated by the model is in close agreement with the analytical solution.

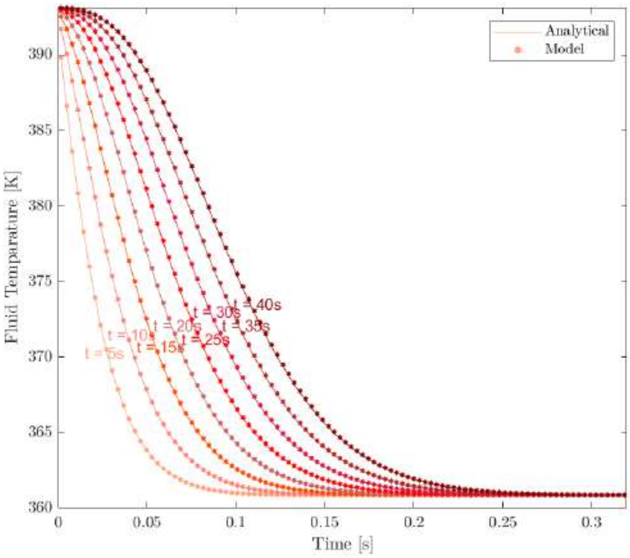

Figure 6.10: Verification of solid - fluid heat transfer code with analytical solution; The temperature profile of solid phase with time.

From the above test it can be concluded that the code pertaining to heat transfer between the phases works as intended.

Heat transfer model validation

The CFD-DEM model developed to evaluate the dynamics of the packed bed utilises correlations to account for the interactions between the solid and fluid phases. As explained in section 4.4, the approach of unresolved flow is favoured while simulating systems with larger amounts of particles. Unfortunately, this introduces a restriction on the ratio of packed bed diameter to particle diameter for predicting the flow. As a result, the the options for experimental base cases for validating the model is narrowed as well.
The experimental setup of Messai et al. (2014) was chosen as the base

case [7]. The experimental setup described in the work of Messai et al. consisted of a packed bed with alumina particles filled into a column of height 0.32m and diameter 0.18m. The setup was initially maintained at 87°C and at time, t=0, hot air at 120°C was blown at 2m/s. In the experiments, a thermocouple was used to measure the temperature of the particles at a set axial position. The information provided is limited to the axial position of the measurements while the exact location of the measurement radially is not known. The model geometry was constructed similar to the experimental setup described. The properties and parameters for the simulation were set accordingly and the simulation was run for a total of 100s. The results of the simulation and the results of the experiments of Mesaai et al. were compared as shown in figure 6.11.

The temperature profile predicted by the model is in close agreement with the experiments. Since the experimental data is limited, a small slice at the mentioned axial position is considered for a fair comparison. The temperature range in that slice is compared to the data from experiments. As seen in figure 6.11, the experimental temperature readings lie well within the range of temperatures recorded in the slice considered. With the above comparison of model and experimental results, it is concluded that the model developed is capable of predicting and evaluating the heat transfer in an adiabatic packed beds.

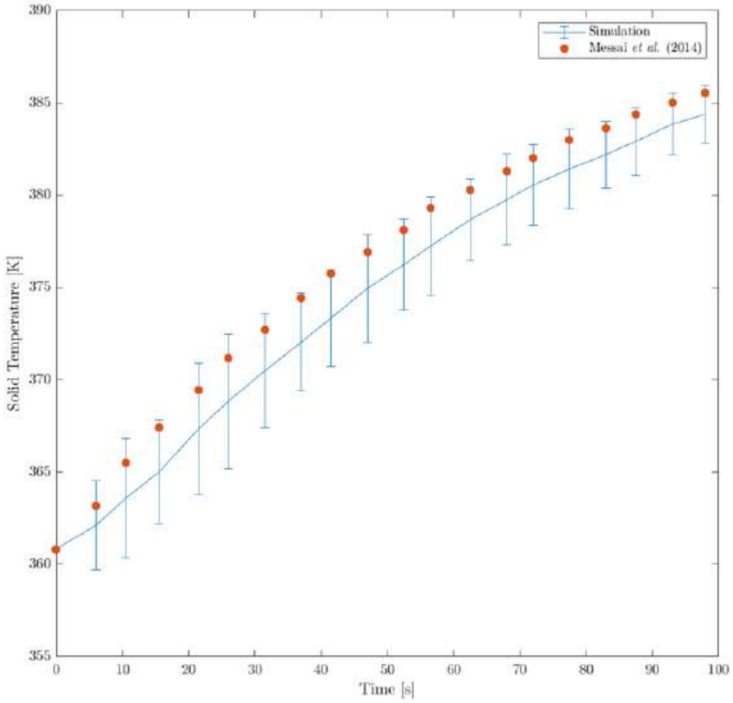

Figure 6.11: Comparing the temperature of solids in experimental results of Messai et al. and the CFD-DEM model results over time [7].

6.2.2 Non adiabatic - Heat transfer through walls

Heat transfer model verification

The heat transfer between the walls and the contents of the system is verified using the analytical solution provided by Yagi et al. (1959) [39]. The equation that describes the heat transfer into a packed bed through the walls is given by equation 6.6.

$$C_p G \frac{\partial T}{\partial l} = k_e \left(\frac{\partial^2 T}{\partial r^2} + \frac{1}{r} \frac{\partial T}{\partial r} \right) \tag{6.6}$$

Boundary condition at inlet:

$$l = 0 \qquad\qquad T = T_0 \tag{6.7}$$

Boundary condition at the inner surface of the wall:

$$r = R, \qquad\qquad k_e \left(\frac{\partial T}{\partial r} \right) = h_w \Big(T_w - T \Big) \tag{6.8}$$

Yagi et al. provides the analytical solution for the PDE with the boundary conditions as specified in equations 6.7 and 6.8,

$$\frac{T_w - T}{T_w - T_0} = 2 \sum_{i=1}^{\infty} \frac{(h_w R/k_e) \cdot J_0(r\xi_i) \cdot e^{-k_e \xi_i^2 l / C_p G}}{\Big[(h_w R/k_e)^2 + (R\xi_i)^2 \Big] \cdot J_0(R\xi_i)} \tag{6.9}$$

where, ξ_i is the root of,

$$(h_w R/k_e) \cdot J_0(R\xi_i) = (R\xi_i) \cdot J_1(R\xi_i) \tag{6.10}$$

To obtain the above analytical solution the following assumptions were made [39]:

1. the temperature difference between solid and fluid is negligible
2. the mass velocity of fluid is uniform across the tube diameter
3. the physical properties of fluid are independent of temperature
4. the effective thermal conductivity is uniform within the bed
5. the axial heat conduction is negligible.

Table 6.3: Properties and parameters of fluids and solids for verification of heat transfer model in a non adiabatic packed bed.

Parameters	**Values**	**Units**
Bed Height	0.36	[m]
Bed Diameter	0.036	[m]
Particle Diameter	$1.08 \cdot 10^{-3}$	[m]
Void Fraction	0.33	[-]
Number of particles	$\sim 33.7 \cdot 10^{5}$	[-]
Cell Size/Particle Dimensions	[2.661 - 5.174]	[-]
Fluid Viscosity	$19.4 \cdot 10^{-6}$	[Pa· s]
Fluid Density	1.103	[kg/m^3]
Fluid Conductivity	$27.86 \cdot 10^{-3}$	[W/m·K]
Fluid Heat Capacity	$1.007 \cdot 10^{3}$	[J/kg·K]
Particle Density	$11.34 \cdot 10^{3}$	[kg/m^{-3}]
Particle Conductivity	33.39	[W/m·K]
Particle Heat Capacity	130	[J/kg·K]
Wall Temperature	373.15	[K]
Inlet Temperature	285.15	[K]
Initial system Temperature	320	[K]
CFD Timestep	$1 \cdot 10^{-3}$	[s]
DEM Timestep	$1 \cdot 10^{-5}$	[s]

The experiment consisted of a packed bed with heating through the walls. The system comprised of lead shots as packing. Air was blown through the system at 12°C while the walls were maintained at 100°C using a steam jacket. The system was designed such that a fixed bed of particles was heated over time through the walls to attain steady state. The parameters and the properties of the experimental setup were applied to the model as shown in table 6.3. The literature states that the system reached steady state in approximately an hour. In order to reduce the computation time, the initial temperature of the particles were increased such that the steady state would be reached faster. The simulation was executed for a run time of 200s where the system appeared to have reached a steady state. The temperature of the air over the z axis was recorded in the simulation and compared with the analytical solution (equation 6.9). The comparison is shown in figure 6.12. The results of the model do not agree with the analytical solution as seen in the figure where the temperature from the simulation is significantly higher.

To further analyse the reason for the disagreement between the model results and analytical solution, the implementation of the model describing the wall heat transfer was checked. The

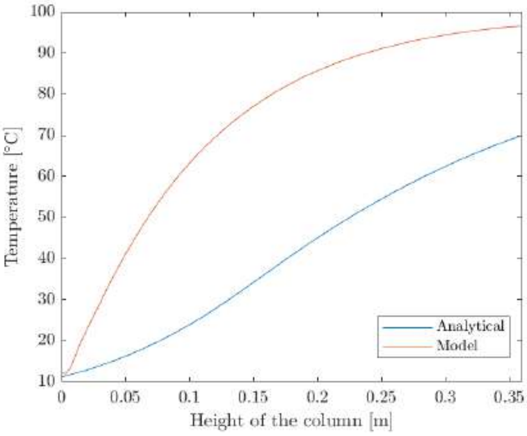

Figure 6.12: Comparing the results of air temperature as predicted by the model and the analytical solution of Yagi et al. (1959).

wall heat transfer calculated by the model was cross checked with manual calculations in certain cells. The model predicts higher heat transfers at the wall as shown in table 6.4. With further investigation on the model, the following were found:

1. An error in implicit calculation for the wall heat flux. Due to this, the magnitude of heat transfer increased with time even though the temperature gradient between the wall and the fluid reduced with time (observed in table 6.4). Therefore the temperature of the bed increases significantly.

2. For the calculation of wall heat coefficient, the Prandtl number is raised to the power (2/3) (equation 4.32). An error occurred during this implementation where (2/3) was declared as an integer and the code executed Prandtl number raised to the power zero.

3. In calculating the particle Reynolds number, a relative velocity between the solid and particle was considered instead of just the fluid velocity.

Table 6.4: Comparison of heat flux calculated by the model with manual calculations.

	t = 1s		**t = 200s**	
Cell ID	$Q_{\text{Simulation}}$	$Q_{\text{Manual calc.}}$	$Q_{\text{Simulation}}$	$Q_{\text{Manual calc.}}$
87	2.0859	0.2513	2.2248	0.0155
144	1.6354	0.2544	1.7448	0.0157
156	1.3296	0.2362	1.4183	0.0146
393	1.4135	0.2478	1.5048	0.0153
511	1.5633	0.2442	1.6662	0.0150
523	2.0970	0.2520	2.2315	0.0155

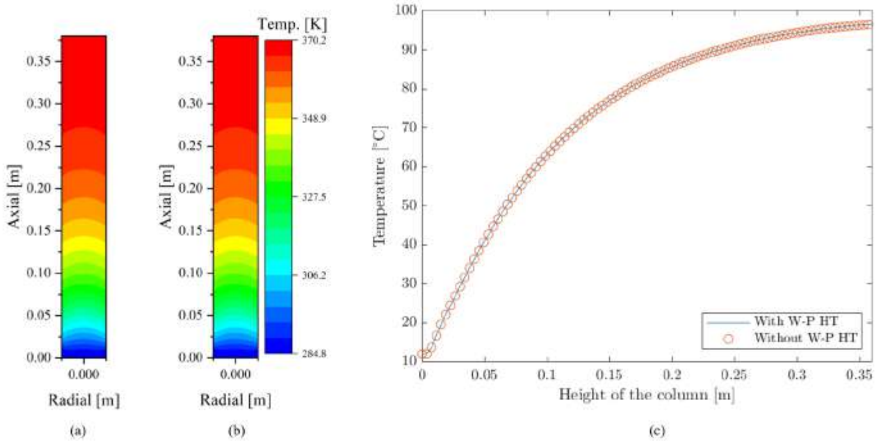

Figure 6.13: (a)Temperature profile of the simulation with wall-particle heat transfer;(b)Temperature profile of the simulation with wall-particle heat transfer;(c)Comparing the results of axial temperature profiles with and without wall-particle heat transfer.

After checking the implementation of fluid-wall heat transfer, the implementation of particle wall heat transfer was checked. Two simulations were conducted where one of the simulation was set according to an assumed procedure to account for the wall particle heat transfer while the other neglected it. The results are shown in figure 6.13 where the temperature profiles are almost exact. This induces the doubt on if the implementation of wall-particle heat transfer is correct. On the other hand, Yagi et al. also states that the influence of wall - particle heat transfer is negligible even during experiments. Hence, this may not be the best case to verify the wall - particle heat transfer.

Fixing the above errors would provide better results. Unfortunately, with the limitation of time, this could not be verified.

6.3 Mass transfer

6.3.1 Single fluid mass transfer model

The model developed to evaluate mass transfer is first verified for a system where a single fluid is present. For verification, a fixed packed bed is considered where the packing consists of spherical particles of benzoic acid. Water enters the system through the bottom and flows through the column. The water has zero concentration of benzoic acid as it enters the system and the particles of benzoic acid starts to dissolve. As the particles dissolve in the water stream, the size of the particles is reduced over time. The flow of water is set such that the resultant Reynolds number ($Re \approx 50$) falls in the flow regime where correlation provided by Gunn to describe solid to fluid mass transfer is found valid.

The particles are added to the bed till a bed porosity of 0.4 is obtained. The fluid is allowed to pass trough the bed and exit the system at the top. The system is run for a total of 60s and parameters used for the simulation are provided in table 6.5.

Table 6.5: Properties and parameters of fluid and solid phases for verifying the mass transfer model.

Parameters	**Values**	**Units**
Bed Height	0.18	[m]
Bed Diameter	0.2	[m]
Particle Diameter	$4.4 \cdot 10^{-3}$	[m]
Void Fraction	0.4	[-]
Cell Size/Particle Dimensions	[2.6909 - 3.7501]	[-]
Fluid Viscosity	$0.89. \cdot 10^{-7}$	[Pa· s]
Fluid Density	997	[kg/m^3]
Diffusivity in water	$9.8 \cdot 10^{-10}$	[m^2/s]
Saturation Concentration	34.14	[kg/m^3]
Particle Density	1321	[kg/m^{-3}]
CFD Timestep	$1 \cdot 10^{-3}$	[s]
DEM Timestep	$1 \cdot 10^{-5}$	[s]

The model verification is done by comparing the results of the model with an analytical solution of one dimensional convection equation with mass transfer between the solid and fluid phases. Further the reduction in particle size due to dissolution is also inspected by an analytical solution. In this case, with a fluid flowing through the column, the diffusive mass transfer is neglected as the Péclet number is found to be Pé = 46719. The following equations were considered for obtaining the analytical solution:

Fluid phase

$$\frac{\partial}{\partial t}(\varepsilon_f C_z) = -\nabla \cdot (\varepsilon_f u_z C_z) + K_m a_p (C_s - C_z) \tag{6.11}$$

Particle size reduction

$$\Delta r_{p,z} = \sqrt[3]{\frac{3}{4\pi\rho_p}\Big[K_m \cdot a_p\big(C_s - C_z\big) \cdot \Delta t\Big]} \tag{6.12}$$

where, K_m is the mass transfer coefficient calculated from the correlation provided by Gunn, a_p is the specific interfacial area of the particle, C_s is the saturation concentration of benzoic acid in water. With the particles dissolving in the fluid over time, the void fraction of the system is calculated as a function of radius. The equations were discretised in one dimension and solved for time, t to obtain the solutions in MATLAB®.

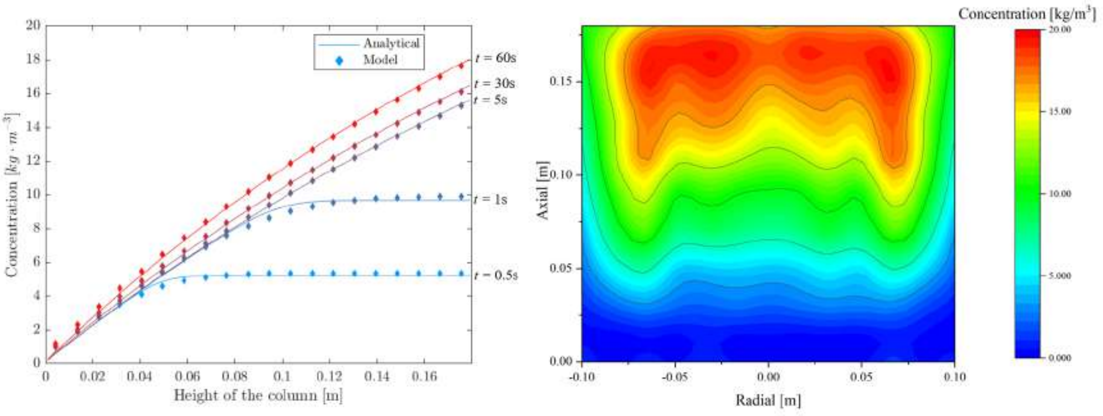

(a) (b)

Figure 6.14: (a) Verification of solid to fluid mass transfer accompanied by convected mass transfer with analytical solution. (b) Axial and radial concentration profile of a system with water flowing through a bed of benzoic acid spherical packing.

Figure 6.14 (a) illustrates the development of concentration profile with time. The simulation results are compared with the results of the analytical solution. The concentration profile obtained from the model is in close agreement with the analytical solution. Further, the concentration profile produced by the model is shown in figure 6.14 (b) representing the radial and axial concentration profile in the bed for a the vertical central plane.

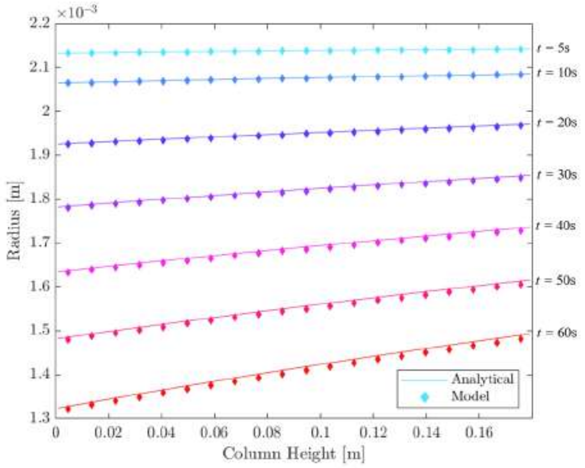

Figure 6.15: Verification of particle size reduction in the model with the analytical solution.

Figure 6.15 shows the change in particle radius over time along the axial direction. The particle radius from the model are averaged over slices with slice thickness equivalent to the distance between the nodes chosen for the analytical solution. It can be observed that the results from the model match the results of the analytical solution closely. Further, it is observed that the particles tend to dissolve at a higher rate near the bottom of the system. This is observed as the concentration gradient at the bottom is maximum (fresh water enters from the bottom). This allows for higher rates of mass transfer between the two phases resulting in higher dissolution. Hence, with these results, it can be concluded that the code predicts mass transfer as intended.

6.3.2 Mass transfer at fluid interface

The model has been developed to account for the mass transfer that occurs at the interface of two fluids. The model is aimed to be applied for a blast furnace where the focus is to prevent the mass transfer at the interface via diffusion. To assess the working of the model, a closed fixed bed with two fluids was considered. The bottom half of the column was filled with water while the top half consisted of air. The fluids were selected such that the particles of the bed dissolve only in one of the fluids.

Table 6.6: Properties and parameters of fluid and solid phases for evaluating the mass transfer at the interface.

Parameters	**Values**	**Units**
Bed Height	0.5	[m]
Bed Diameter	0.2	[m]
Particle Diameter	$4.4 \cdot 10^{-3}$	[m]
Void Fraction	0.4	[-]
Diffusivity in water	$9.8 \cdot 10^{-10}$	[m^2/s]
Diffusivity in air	$1.2 \cdot 10^{-7}$	[m^2/s]
Saturation Concentration in water	34.14	[kg/m^3]
Saturation Concentration in air	$1 \cdot 10^{-3}$	[kg/m^3]
CFD Timestep	$1 \cdot 10^{-3}$	[s]
DEM Timestep	$1 \cdot 10^{-5}$	[s]

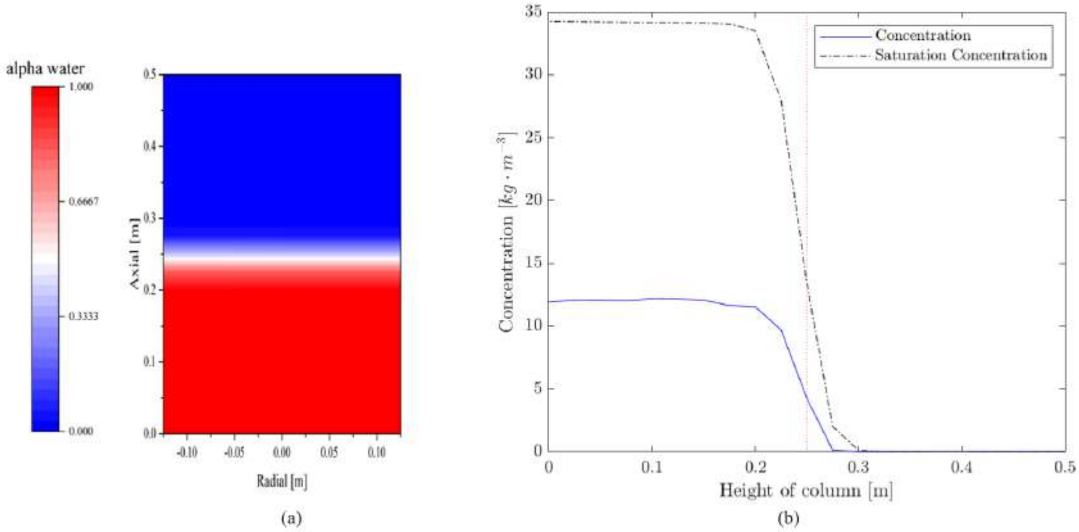

Figure 6.16: (a) Volume fraction of the fluids, water and air in the system to check for the mass transfer at the interface via diffusion; (b) Concentration profile in the column at the end of 20s; The saturation concentration in the system is illustrated to assess the concentration profile; The red dotted line represents the interface.

For this purpose, a bed of benzoic acid spheres were added to a column till void fraction reached 0.4. The particles were introduced into the bed and was allowed to settle with gravity forming an irregular packing of the bed. The volume fractions of the fluids and the interface is shown in figure 6.16 (a). The initial concentrations of both the fluids was set to zero. With time, the benzoic acid particles dissolve in water and the concentration increases. Further, diffusion at the interface was restricted using the correction as described in section 4.6.1 with Henry's constant for air set to zero. With no particle dissolution and interfacial diffusion in air, the concentration over time was expected to remain close to zero. The system had no flow through it in order to focus on diffusion. The simulation was run for a total of 20 seconds with parameters described in table 6.6.

In figure 6.16 (b), it is observed that the concentration in water is increasing while the concentration in air is almost zero. The concentration profile in the cells close to the interface show a significant deviation from the bulk of the fluid. This deviation is observed as the interface described in the system is not sharp (also seen in figure 6.16 (a)) and therefore provides a smeared concentration profile in the cells close to the interface. The overall concentration profile at the bulk of the fluids are as expected. The concentration in water increases with time while the concentration in bulk of air remains zero. A better interface representation would result in a more precise drop in concentration profile at the interface. Further, the concentration profile throughout the system remains well under the saturation concentration of the system.

Chapter 7

Conclusions

This project was aimed at understanding the dynamics of the blast furnace (BF) hearth. The research was focused on three main aspects, the fluid flow, heat and mass transport inside the hearth.

For the flow, experiments and simulation were done to complement eachother and together provided a broad analysis. An experimental setup was employed where the BF hearth was closely represented with inclusion of burden force and raceways. During experiments, the influence of inflow rates into the hearth was emphasised. As expected, with higher inflow rates, the frequency of tapping increased. The MPT results also revealed that particles inside the bed migrated over time and were influenced by the inflow rates. The higher frequencies of tapping provided more room for rearrangement of the bed, allowing particle migration. With more rearrangement, the porosity of the bed increases allowing for a better seepage and lesser circumferential flows (i.e. less stress on the walls). Further, during the migration, debris trapped in the deadman would reach the slag with relative ease.

The model was validated using experimental data. The flow patterns inside the hearth could not be analysed during the experiments. Hence, with the help of simulation fluid flow inside the hearth was analysed. First, it was interesting to observe the well-documented phenomenon of circumferential flow and higher fluid velocities at the coke free spaces. Next, the influence of inflow rates was analysed using time averaged fluid velocities. With higher frequencies of tapping, the time averaged fluid velocity increased as expected. Further the simulation shows that the void fraction in the bed increases with higher frequencies of tapping.

Heat is transferred between the coke particles and the molten metal in a BF hearth alongside the heat transfer between the walls. The model developed to analyse the particle-fluid heat transfer with fluid conduction provided good agreements with the experimental data. However, during the modelling of heat transfer through the walls few problems were encountered and the model shows significant deviation from the experimental data. The heat transfer through the walls of the hearth is an important aspect in BF hearth operation and therefore its modelling requires further attention.

Coke particles in the blast furnace dissolve into the molten iron. To predict this phenomenon, a mass transfer model was developed in analogous to the heat transfer model. The method to evaluate the mass transfer between the particles and fluid remained similar to the heat transfer methods. On the other hand, diffusion through the fluid was modified to include a correction flux, which accounts for the diffusion at the interface of two fluids. As a coke particle dissolves in the molten metal, the size of the particle reduces. This brings in a change in the void fraction of the deadman. As explained before, the void fraction of the bed plays a vital role during tapping. Hence, the model developed was also successful in predicting the particle dissolution.

Summing up, through the experiments and simulations, an interesting process of particle migration was observed in a moving packed bed. Combing the results of experiments and simulations, the influence of inflow rates on bed dynamics was analysed. Lastly, a model was developed to evaluate the heat and mass transfer of a packed bed that could be adapted to evaluate a blast furnace hearth.

Chapter 8

Future perspective

Firstly, further investigation is needed regarding the heat transfer in a non adiabatic packed bed. For a blast furnace, the heat transfer through the walls is an important aspect. To reduce the magnitude of thermo-mechanical stress from the molten metal, the walls of the blast furnace hearth is cooled to form a layer of solid iron called the skull layer. For any further analysis of the skull layer or the stress on the walls, the heat transfer through the walls must be established and evaluated in the model. During further investigations, the implementation of DEM based heat transfer between the particles and the wall must be done evaluated carefully.

Further, the model developed is applied currently to small packed beds only. The final goal of the model is to be adapted to a large scale blast furnace. The enormous domain of simulation with a large number of particles could prove computationally challenging. An approach to simulate the large scale blast furnace efficiently would be through coarse-graining. The methods for coarse-graining of a liquid-solid system must be evaluated. Further, evaluating the significance and implementing the interacting forces (steady and unsteady) between the phases in a coarse-grained simulation would be interesting. The process of coarse-graining the heat and mass transfer models to ease the computation would prove helpful.

When two particles are in contact, the transfer of heat between the particles can occur through the area of contact as well as through the thin layer of fluid between the particles. Usually, the heat transfer through these thin fluid films are neglected as the thermal conductivity of the fluid is insignificant compared to the solid particles (as seen in the heat transfer tests of air blown packed beds). But in a blast furnace, the thermal conductivity of molten iron is greater than the thermal conductivity of the solid coke particles. Hence, it would be compelling to analyse the heat transfer through this fluid film.

Acknowledgement

Firstly, I would like to thank Prof. Hans Kuipers for providing me the opportunity to work on a very interesting and challenging project in the group of SMR (Multiphase Reactor Group). I would like to thank Prof. Kuipers and Dr. Kay Buist for all their input and advice during the progress meetings. Furthermore, I thank Dr. Giulia Finotello for being a part of the graduation committee.

I cannot express my gratitude enough towards Tim Nijssen for all his help. Tim is one of the most patient and the nicest person I have ever met who always found time to help his students. He was the ideal daily supervisor and I could approach him for anything regarding fluid dynamics, image rendering or any other matter. I thank him for his help through out the project.

I would also like to thank Indy, Nikolaj and Danny who kept me company in the office aptly named “CFTeaHouse”. I enjoyed every discussions we had while having *Tea*. Further, I would like to thank Herbert and Thuijs for their help in setting up the experiments. I also thank my friends in the university who helped in taking my mind off the project during breaks.

Lastly, I thank my family, Manjunath, Rajashree and Vishakha for their support during my education. I appreciate their moral support that helped me during my time here in Eindhoven, home away from home.

Bibliography

[1] Worldsteel Association, "World Steel in Figures 2019," Tech. Rep., 2019.

[2] R. Parra, L. F. Verdeja, M. F. Barbés, and C. Goñi, "Furnace lining analysis and design by mathematical and physicochemical modeling," *2006 TMS Fall Extraction and Processing Division: Sohn International Symposium*, vol. 8, no. August, pp. 561–575, 2006.

[3] Y. Omori, *Blast furnace phenomena and modelling.* Elsevier Applied Science, 1987.

[4] J. I. Yagi, "Mathematical Modeling of the Flow of Four Fluids in a Packed Bed," *ISIJ International*, vol. 33, no. 6, pp. 61–70, 1993.

[5] M. Vångö, S. Pirker, and T. Lichtenegger, "Unresolved CFD–DEM modeling of multiphase flow in densely packed particle beds," *Applied Mathematical Modelling*, vol. 56, pp. 501–516, April 2018.

[6] M. Swartling, B. Sundelin, A. Tilliander, and P. G. Jönsson, "Heat Transfer Modelling of a Blast Furnace Hearth," *Steel research international*, vol. 81, no. 3, pp. 186–196, mar 2010.

[7] S. Messai, M. E. Ganaoui, J. Sghaier, and A. Belghith, "Experimental study of the convective heat transfer coefficient in a packed bed at low reynolds numbers," *Thermal Science*, vol. 18, no. 2, pp. 443–450, 2014.

[8] H. Kurosawa, S. Matsuhashi, S. Natsui, T. Kon, S. Ueda, R. Inoue, and T. Ariyama, "DEM-CFD model considering softening behavior of ore particles in cohesive zone and gas flow analysis at low coke rate in blast furnace," *ISIJ International*, vol. 52, no. 6, pp. 1010–1017, 2012.

[9] M. Geerdes, H. Toxopeus, and C. van der. Vliet, *Modern Blast Furnace Ironmaking.* IOS Press, 2009.

[10] A. Adema, "DEM-CFD Modelling of the ironmaking blast furnace," Doctoral Thesis, Delft University of Technology, 2014.

[11] J. Brulin, F. Roulet, R. Mcnally, and M. Micollier, "Latest Evolution in Blast Furnace Hearth thermo-Mechanical Stress Modelling The BF hearth," *InSteelCon*, pp. 1–7, 2011.

[12] S. N. Silva, F. Vernilli, S. M. Justus, O. R. Marques, A. Mazine, J. B. Baldo, E. Longo, and J. A. Varela, "Wear mechanism for blast furnace hearth refractory lining," *Ironmaking & Steelmaking*, vol. 32, no. 6, pp. 459–467, 2005.

[13] L. Shao, "Model - Based Estimation Of Liquid Flows In The Blast Furnace Hearth," Ph.D. dissertation, Åbo Akademi University, 2013.

[14] A. Adema, Y. Yang, and R. Boom, "Coupled DEM – CFD modelling of the ironmaking blast furnace," *Seventh International Conference on CFD in the Minerals and Process Industries CSIRO*, vol. 2, no. December, pp. 1–6, 2009.

[15] D. Pan, Z. Jiang, Z. Chen, W. Gui, Y. Xie, and C. Yang, "Temperature measurement method for blast furnace molten iron based on infrared thermography and temperature reduction model," *Sensors (Switzerland)*, vol. 18, no. 11, 2018.

[16] D. Gathergood, Jones, and Goldring, "Progressive Reduction Of Burden In The Blast Furnace," Tech. Rep., 1989.

[17] X. Dong, A. Yu, J.-i. Yagi, and P. Zulli, "Modelling of Multiphase Flow in a Blast Furnace: Recent Developments and Future Work," *ISIJ International*, vol. 47, no. 11, pp. 1553–1570, nov 2007.

[18] P. R. Austin, H. Nogami, and J.-i. Yagi, "Prediction of Blast Furnace Performance with Top Gas Recycling." *ISIJ International*, vol. 38, no. 3, pp. 239–245, 1998.

[19] J. A. de Castro, H. Nogami, and J.-i. Yagi, "Transient Mathematical Model of Blast Furnace Based on Multi-fluid Concept, with Application to High PCI Operation." *ISIJ International*, vol. 40, no. 7, pp. 637–646, 2000.

[20] S. A. Zaïmi, T. Akiyama, J. B. Guillot, and J. I. Yagi, "Sophisticated multi-phase multi-flow modeling of the blast furnace," *ISIJ International*, vol. 40, no. 4, pp. 322–331, 2000.

[21] S. J. Chew, P. Zulli, and A. Yu, "Mathematical Modeling of Iron and Steel Making Processes. Modelling of Liquid Flow in the Blast Furnace. Application in a Comprehensive Blast Furnace Model." *ISIJ International*, vol. 41, no. 10, pp. 1122–1130, 2001.

[22] Z. Y. Zhou, H. P. Zhu, A. B. Yu, B. Wright, and P. Zulli, "Discrete particle simulation of gas-solid flow in a blast furnace," *Computers and Chemical Engineering*, vol. 32, no. 8, pp. 1760–1772, aug 2008.

[23] P. A. Cundall and O. D. Strack, "A discrete numerical model for granular assemblies," *Geotechnique*, vol. 29, no. 1, pp. 47–75, 1979.

[24] K. Tanaka, M. Nishida, T. Kunimochi, and T. Takagi, "Numerical and experimental studies for the impact of projectiles on granular materials," in *Handbook of Powder Technology.* Elsevier, 2001, vol. 10, pp. 263–270.

[25] C. Kloss, C. Goniva, G. Aichinger, and S. Pirker, "Comprehensive DEM-DPM-CFD simulations-Model Synthesis, experimental validation and scalability," in *Seventh International Conference on CFD in the Minerals and Process Industries, CSIRO*, Melbourne, Australia, 2009.

[26] C. Kloss, C. Goniva, A. Hager, S. Amberger, and S. Pirker, "Models, algorithms and validation for opensource DEM and CFD-DEM," *Progress in Computational Fluid Dynamics*, vol. 12, no. 2-3, pp. 140–152, 2012.

[27] S. Radl, T. Forgber, A. Aigner, and C. Kloss, "Parscale - An open-source library for the simulation of intra-particle heat and mass transport processes in coupled simulations," *Proceedings of the 4th International Conference on Particle-Based Methods - Fundamentals and Applications, PARTICLES 2015*, no. February 2017, pp. 117–127, 2015.

[28] S. Natsui, S. Ueda, H. Nogami, J. Kano, R. Inoue, and T. Ariyama, "Analysis on non-uniform gas flow in blast furnace based on DEM-CFD combined model," *Steel Research International*, vol. 82, no. 8, pp. 964–971, 2011.

[29] M. Vangö, S. Pirker, and T. Lichtenegger, "CFD-DEM modelling of blast furnace tapping," *CFD 2017*, 2017.

[30] Z. Miao, Z. Zhou, A. B. Yu, and Y. Shen, "CFD-DEM simulation of raceway formation in an ironmaking blast furnace," *Powder Technology*, vol. 314, pp. 542–549, jun 2017.

[31] F. Bambauer, S. Wirtz, V. Scherer, and H. Bartusch, "Transient DEM-CFD simulation of solid and fluid flow in a three dimensional blast furnace model," *Powder Technology*, vol. 334, pp. 53–64, 2018.

[32] G. Wei, H. Zhang, X. An, B. Xiong, and S. Jiang, "CFD-DEM study on heat transfer characteristics and microstructure of the blast furnace raceway with ellipsoidal particles," *Powder Technology*, vol. 346, pp. 350–362, 2019.

[33] B. Chaudhuri, F. J. Muzzio, and M. S. Tomassone, "Modeling of heat transfer in granular flow in rotating vessels," *Chemical Engineering Science*, vol. 61, no. 19, pp. 6348–6360, 2006.

[34] C. S. Bu, D. Y. Liu, X. P. Chen, C. Liang, Y. F. Duan, and L. B. Duan, "Modeling and coupling particle scale heat transfer with DEM through heat transfer mechanisms," *Numerical Heat Transfer; Part A: Applications*, vol. 64, no. 1, pp. 56–71, 2013.

[35] E. Tsotsas, "Particle-particle heat transfer in thermal DEM: Three competing models and a new equation," *International Journal of Heat and Mass Transfer*, vol. 132, pp. 939–943, 2019.

[36] P. N. Baptista, F. A. Oliveira, J. C. Oliveira, and S. K. Sastry, "Dimensionless analysis of fluid-to-particle heat transfer coefficients," *Journal of Food Engineering*, vol. 31, no. 2, pp. 199–218, 1997.

[37] D. Gunn, "Transfer of heat or mass to particles in fixed and fluidised beds," *International Journal of Heat and Mass Transfer*, vol. 21, no. 4, pp. 467–476, apr 1978.

[38] S. Yagi and D. Kunii, "Studies on effective thermal conductivities in packed beds," *AIChE Journal*, vol. 3, no. 3, pp. 373–381, 1957.

[39] S. Yagi and N. Wakao, "Heat and mass transfer from wall to fluid in packed beds," *AIChE Journal*, vol. 5, no. 1, pp. 79–85, mar 1959.

[40] N. Wakao and K. Kato, "Effective Thermal Conductivity of Packed Beds," *Journal of Chemical Engineering of Japan*, vol. 2, no. 1, pp. 24–33, 1969.

[41] P. Zehner and E. U. Schlünder, "Wärmeleitfähigkeit von Schüttungen bei mäßigen Temperaturen," *Chemie Ingenieur Technik*, vol. 42, no. 14, pp. 933–941, 1970.

[42] E. Tsotsas and H. Martin, "Thermal conductivity of packed beds: A review," *Chemical Engineering and Processing*, vol. 22, no. 1, pp. 19–37, 1987.

[43] R. Bauer and E. U. Schluender, "Effective radial thermal condictivity of packings in gas flow. Part II. Thermal conductivity of the packing fraction without gas flow," *International Chemical Engineering*, vol. 18, no. 2, pp. 189 – 204, 1978.

[44] C. O. Castillo-Araiza, H. Jiménez-Islas, and F. López-Isunza, "Heat-transfer studies in packed-bed catalytic reactors of low tube/particle diameter ratio," *Industrial and Engineering Chemistry Research*, vol. 46, no. 23, pp. 7426–7435, 2007.

[45] M. De Beer, P. G. Rousseau, and C. G. Du Toit, "A review of methods to predict the effective thermal conductivity of packed pebble beds, with emphasis on the near-wall region," *Nuclear Engineering and Design*, vol. 331, no. March, pp. 248–262, 2018.

[46] M. Nijemeisland and A. G. Dixon, "CFD Study of Fluid Flow and Wall Heat Transfer in a Fixed Bed of Spheres," *AIChE Journal*, vol. 50, no. 5, pp. 906–921, 2004.

[47] S. Yagi and D. Kunii, "Studies on heat transfer near wall surface in packed beds," *AIChE Journal*, vol. 6, no. 1, pp. 97–104, 1960.

[48] A. G. Dixon, "Wall and particle-shape effects on heat transfer in packed beds," *Chemical Engineering Communications*, vol. 71, no. 1, pp. 217–237, sep 1988.

[49] S. Kumar, "Heat transfer analysis and estimation of refractory wear in an iron blast furnace hearth using finite element method," *ISIJ International*, vol. 45, no. 8, pp. 1122–1128, 2005.

[50] S. J. Gdula, R. Bialecki, K. Kurpisz, A. Nowak, and A. Sucheta, "Mathematical model of steady state heat transfer in blast furnace hearth and bottom." *Transactions of the Iron and Steel Institute of Japan*, vol. 25, no. 5, pp. 380–385, 1985.

[51] Y. Zhang, R. Deshpande, D. F. Huang, P. Chaubal, and C. Q. Zhou, "Numerical analysis of blast furnace hearth inner profile by using CFD and heat transfer model for different time periods," *International Journal of Heat and Mass Transfer*, vol. 51, no. 1-2, pp. 186–197, jan 2008.

[52] S. Kumar and V. S. Bisht, "2D modelling and simulation of heat transfer in blast furnace hearth using ANSYS," in *Advances in Intelligent Systems and Computing*, vol. 624. Springer Verlag, 2018, pp. 1051–1063.

[53] A. Preuer, J. Winter, and H. Hiebler, "Computation of the erosion in the hearth of a blast furnace," *Steel Research*, vol. 63, no. 4, pp. 147–151, apr 1992.

[54] K. X. Jiao, J. L. Zhang, Z. J. Liu, C. L. Chen, and Y. X. Liu, "Analysis of blast furnace hearth sidewall erosion and protective layer formation," *ISIJ International*, vol. 56, no. 11, pp. 1956–1963, 2016.

[55] K. Takatani, T. Inada, and K. Takata, "Mathematical model for transient erosion process of blast furnace hearth," *ISIJ International*, vol. 41, no. 10, pp. 1139–1145, 2001.

[56] H. W. Gudenau, J. P. Mulanza, and D. G. R. Sharma, "Carburization of hot metal by industrial and special cokes," *Steel Research*, vol. 61, no. 3, pp. 97–104, 1990.

[57] J. Post, T. Peeters, Y. Yang, and M. Reuter, "Hot Metal Flow in the Blast Furnace Hearth: Thermal and Carbon Dissolution Effects on Buoyancy. Flow and Refractory Wear," *3rd International Conference on CFD in the Minerals and Process Industries*, no. December, pp. 433–440, 2003.

[58] M. A. Reuter, J. R. Post, and Y. Yang, "Hot metal flow in the hearth of a blast furnace : Influence of dynamic changes deadman porosity due to coke dissolution and coke size changes," in *The 5th European Coke and Ironmaking Congress - 5th ECIC*, no. June. he 5th European Coke and Ironmaking Congress - 5th ECIC, 2005.

[59] K. A. Buist, A. C. van der Gaag, N. G. Deen, and J. A. M. Kuipers, "Improved magnetic particle tracking technique in dense gas fluidized beds," *AIChE Journal*, vol. 60, no. 9, pp. 3133–3142, sep 2014.

[60] H. Hemida, "OpenFOAM tutorial : Free surface tutorial using interFoam and rasInterFoam Available solvers in OpenFOAM," pp. 1–31, 2008.

[61] R. Beetstra, M. A. van der Hoef, and J. A. M. Kuipers, "Drag force of intermediate Reynolds number flow past mono- and bidisperse arrays of spheres," *AIChE Journal*, vol. 53, no. 2, pp. 489–501, feb 2007.

[62] R. Mei, "An approximate expression for the shear lift force on a spherical particle at finite reynolds number," *International Journal of Multiphase Flow*, vol. 18, no. 1, pp. 145–147, 1992.

[63] E. Loth, "Lift of a Spherical Particle Subject to Vorticity and/or Spin," *AIAA Journal*, vol. 46, no. 4, pp. 801–809, 2008.

[64] C. T. Crowe, J. D. Schwarzkopf, M. Sommerfeld, and Y. Tsuji, *Multiphase Flows with Droplets and Particles*, second edi ed. CRC Press Taylor & Francis Group, 2012.

[65] M. Parmar, S. Annamalai, S. Balachandar, and A. Prosperetti, "Differential formulation of the viscous history force on a particle for efficient and accurate computation," *Journal of Fluid Mechanics*, vol. 844, pp. 970–993, 2018.

[66] T. M. J. Nijssen, H. A. M. Kuipers, J. V. D. Stel, and A. T. Adema, "Complete liquid-solid momentum coupling for unresolved CFD-DEM simulations," 2020, Submitted to International Journal of Multiphase Flow.

[67] J. Meseguer, I. Pérez-Grande, and A. Sanz-Andrés, "Thermal radiation heat transfer," *Spacecraft Thermal Control*, vol. Ill, pp. 73–86, 2012.

[68] J. Kuneš, "Thermomechanics," in *Dimensionless Physical Quantities in Science and Engineering.* Elsevier, 2012, pp. 173–283.

[69] E. W. Weisstein, "Sphere-Sphere Intersection."

[70] K. A. Buist, B. J. Backx, N. G. Deen, and J. A. Kuipers, "A combined experimental and simulation study of fluid-particle heat transfer in dense arrays of stationary particles," *Chemical Engineering Science*, vol. 169, pp. 310–320, 2017.

[71] M. Syamlal and D. Gidaspow, "Hydrodynamics of fluidization: Prediction of wall to bed heat transfer coefficients," *AIChE Journal*, vol. 31, no. 1, pp. 127–135, jan 1985. [Online]. Available: http://doi.wiley.com/10.1002/aic.690310115

[72] Y. Haroun, D. Legendre, and L. Raynal, "Volume of fluid method for interfacial reactive mass transfer: Application to stable liquid film," *Chemical Engineering Science*, vol. 65, no. 10, pp. 2896–2909, may 2010.

[73] D. Bothe, M. Kröger, A. Alke, and H. J. Warnecke, "VOF-based simulation of reactive mass transfer across deformable interfaces," *Progress in Computational Fluid Dynamics*, vol. 9, no. 6-7, pp. 325–331, 2009.

[74] N. W. Jones, "Kinetics of carbon dissolution in Fe-C alloy at 1550 C," *Ironmaking and Steelmaking*, vol. 25, no. 6, pp. 460–465, 1998.

[75] TwinCAT 3, "TC3 Controller Toolbox," pp. 1–180, 2019.

[76] M. W. Chapman, R. J. Nightingale, and B. J. Monaghan, "Influence of coke ash on blast furnace hearth behaviour," *CHEMECA 2011: Australasian Conference on Chemical Engineering*, pp. 1–14, 2011.

[77] R. B. Bird, W. E. Stewart, and E. N. Lightfoot, *Transport Phenomena, Wiley International edition*, revised 2n ed. John Wiley & Sons, 2006.

[78] K. Shibata, Y. Kimura, M. Shimizu, and S.-i. Inaba, "Dynamics of dead-man coke and hot metal flow in a blast furnace hearth." *ISIJ International*, vol. 30, no. 3, pp. 208–215, mar 1990.

[79] C. E. Huang, S. W. Du, and W. T. Cheng, "Numerical investigation on hot metal flow in blast furnace hearth through CFD," *ISIJ International*, vol. 48, no. 9, pp. 1182–1187, 2008.